

Contents lists available at ScienceDirect

Additive Manufacturing

journal homepage: www.elsevier.com/locate/addma



Research paper

Efficient computational framework for image-based micromechanical analysis of additively manufactured Ti-6Al-4V alloy

M. Pinz a, S. Storck b, T. Montalbano b, B. Croom b, N. Salahudin b, M. Trexler b, S. Ghosh c,*

- ^a Civil and Systems Engineering, Johns Hopkins University, Baltimore, MD 21218, United States of America
- ^b Johns Hopkins Applied Physics Laboratory, Laurel, MD 20723, United States of America
- ^c Civil & Systems, Mechanical and Materials Science & Engineering, Johns Hopkins University, Baltimore, MD 21218, United States of America

ARTICLE INFO

Keywords: Additively manufactured Ti-6Al-4V Statistically equivalent microstructural volume element (SEMVE) α lath variants Effective crystal plasticity model Self-consistent boundary conditions

ABSTRACT

The increase in additively manufactured (AM) Ti-6Al-4V alloys in high-performance industrial applications has necessitated the development of robust computational models that can aid in their qualification and certification. Physics-based micromechanical models, relating the AM-processed material microstructure and defect state with the overall material response and life, can play an important role in reducing uncertainty in component behavior and increasing acceptance. Motivated by this need, the present paper develops a novel image-based crystal plasticity finite element model (CPFEM) for efficient micromechanical simulation of the additively manufactured Ti-6Al-4V alloy, whose Widmanstätten microstructure is characterized by 12 HCP α lath variants in the parent β grain. A unique feature of this work is the creation of an efficient crystal plasticity framework for the parent β grain polycrystalline ensembles with parametric representation of the α lath statistics of size, shape, orientation, and crystallography. This statistical representation is expected to significantly enhance its efficiency over models that represent each α lath explicitly in the microstructure. Defects in the form of voids are represented at two scales. The smaller voids in the microstructure are manifested as porosity or void volume fraction distribution in the crystal plasticity model. Larger voids are represented explicitly in the statistically equivalent microstructural volume element (SEMVE) model. The models are built from experimentally acquired electron back scatter diffraction (EBSD) and micro-focus X-ray computed tomography (XCT) images and calibrated and validated with mechanical testing data. This paper extends the developments in Pinz et al. (2022) through the development of a special self-consistent boundary condition in the context of a concurrent model to overcome limitations of periodicity boundary conditions. The concurrent model embeds the SEMVE in a homogenized exterior domain represented by a rate-dependent isotropic plasticity model. Parametric studies are conducted to comprehend the effect of void size, shape and orientation on the overall material response.

1. Introduction

Laser powder bed fusion (LPBF) and electron beam powder bed fusion (EBPBF) are commonly used additive manufacturing (AM) methods for fabricating metallic components from powder-based feedstock [1]. While these methods have made tremendous advances, their general adoption in major applications has been impaired due to the inability to qualify and certify AM-processed materials and components [2]. Inconsistencies in material behavior and life due to variations in the microstructural morphology and defects, such as porosity and surface imperfections, are largely responsible for these impediments [3, 4]. Effective computational models that can relate the microstructure to the overall response of these materials must be developed to address these issues.

The additively manufactured Ti-6Al-4V alloy, studied in this paper, has shown considerable promise for high-performance, mission-critical components with complex topological configurations. Its microstructure consists of HCP lattice-based α phase and BCC lattice-based β phase, whose volume fractions are dependent on the material composition and heat treatment. In the LPBF process, the powder feedstock is first melted. Upon re-solidification, the material first assumes the β phase till it cools below the β transus temperature that is approximately 950°C. Below this temperature, α laths nucleate and grow to proliferate the entire microstructure. The crystallographic orientation of each of the 12 α laths is related to that of the parent β grain through a unique Burgers relationship, giving rise to 12 unique variants. The high rates of cooling in AM processes lead to frequent nucleation in the bulk,

E-mail address: sghosh20@jhu.edu (S. Ghosh).

^{*} Corresponding author.

resulting in smaller α laths (than other conventional processes), and Widmanstätten or basketweave type microstructures. Build parameters such as hatch spacing, laser power, scan speed, etc., greatly affect the material thermal history and consequently the morphology of the α phase.

While the literature on image-based crystal plasticity models of conventionally processed α/β phase Ti-6Al-4V alloy is quite extensive viz. [5-10], there have been relatively fewer developments for AMprocessed Ti-6Al-4V alloy with Widmanstätten microstructures [11]. In part, this was due to the difficulty of obtaining 3D virtual representations of the α lath microstructure. The recent years are however seeing an emergence of crystal plasticity-based micromechanical modeling of AM-processed Ti-6Al-4V alloy with complex microstructures. For example, the effects of powder and processing on porosity and properties have been analyzed in [12], grain-level residual stresses have been incorporated in crystal plasticity models in [13], phasefield and crystal plasticity models have been integrated for predicting structure-property relations in [14], anisotropic tensile behavior has been explored in [15], and tensile properties have been predicted in [16]. Physics-based approaches for generating virtual instantiations of Widmanstätten microstructures have been pursued in [17-20] by varying the energy of formation for different crystallographic orientations as a function of the material stress state. While these methods are promising, many require highly refined spatial resolutions that make them computationally intensive for larger simulation volumes.

Recently, an effective crystal plasticity model representing the microstructure of additively manufactured Ti-6Al-4V alloy along with porosity distributions has been developed in [21]. This model circumvents the need to construct explicit α laths by introducing a parametric representation of the statistics of size, shape, and variant volume fraction of each of the 12 α lath variants in the crystal plasticity constitutive law. The overall mechanical response of all α lath variants is manifested through a volume fraction-based weighted averaging rule. A statistically equivalent microstructural volume element (SEMVE) is constructed containing explicit representations of the β grain morphology, with α lath descriptors assigned to each β grain. The Burgers relation then describes the crystallography of the α laths with respect to the explicitly defined β grain. Perspectives on the micromechanical modeling of the impact of porosity variations in additively manufactured metal microstructures have also been given in [22].

The present paper extends the developments in [21] to conduct a parametric study of the effect of defects in the microstructure that are inherent to the additively manufactured Ti-6Al-4V alloy. Microstructural voids and porosity are observed in two forms, viz. key-holing (KH) and lack of fusion (LoF) voids. KH is typically caused by an excess of energy in a localized area, resulting in gas pockets being trapped while the material is still in a molten state [23]. LoF is the result of insufficient energy density, resulting in feedstock that has not fused. By varying the material processing conditions such as beam speed, power, beam width, raster pattern, etc., the material processing conditions can be tightly controlled to minimize both types of voids and porosity. However, even under ideal processing conditions, both types of porosity simultaneously exists, highlighting the difficulty of eliminating porosity altogether. While many studies have focused on how to reduce porosity in AM processed materials [24], less research has been done on modeling the interplay between the microstructure and voids. The size distribution of non-densified defects spans orders of magnitude, from a few µm to over 100 µm. In this paper, different modeling approaches are proposed for the defects depending on their size. The micro-focus X-ray computed tomography (XCT) scanner has a maximum resolution corresponding to a defect size of 24 µm. Defects that are less than 24 µm are represented in the form of porosity or void volume fraction and are incorporated as an evolving parameter in the constitutive relation as developed in [25]. For defects larger than 24 µm the voids are represented explicitly in the micromechanical models. An important feature is the use of self-consistent boundary

conditions [26,27] on the micromechanical domains to avoid over-constraining issues with imposed periodicity boundary conditions. The interaction between the α Widmanstätten microstructure and voids is critical to the material performance and life and is accounted for in this micromechanical model for reliable predictions.

An overview of material description, build processes, mechanical testing experiments, and image acquisition methods is given in Section 2. In Section 3, the image processing pipeline and cleanup procedures, including void and porosity identification are discussed. The effective crystal plasticity model, parametrically incorporating the effect of the α lath variants and the porosity evolution, is discussed in Section 4. The results of simulations with the model are analyzed in Section 6. Section 7 summarizes the developments in this paper.

2. Overview of the material, manufacturing process, and mechanical testing

The AM-processed Ti-6Al-4V alloy (5.82% by weight Al, 4% V, 0.2% Fe, 0.1% O and the rest Ti) modeled in this study has a Widmanstätten microstructure with α/β phases. The microstructural electron backscatter diffraction (EBSD) scan shows $\geq 98\%$ α phase area fraction, implying that nearly all deformation will occur on HCP slip systems. The α phase is characterized by interlocking laths that can be adequately approximated by as ellipsoids. The Burgers relationships $(0001)_{\alpha} \parallel (101)_{\beta}$ and $[11\bar{2}0]_{\alpha} \parallel [\bar{1}11]_{\beta}$ [28] describes the crystallography of each α variant with respect to the parent β grain.

2.1. Material build parameters

The samples used in this study are processed on an EOS M290 metal laser powder bed fusion (LPBF) system in argon shielding gas using a 400w yb-fiber laser with a spot size of 100 μm . Grade 5 Ti powder is procured from EOS with chemical composition in accordance with ASTM F1472 and ASTM F2924. Using a camsizer particle size analyzer, the powder size distribution is determined to fall within the specified range 10 – 63 μm particle size distribution with a mean size 36.7 μm, and the 10th and 90th percentile sizes being 22.4 μm and 46.3 μm respectively. Two different processing conditions are employed in this study, viz. (i) a control set referred to as Stock, and (ii) a set designed to generate keyhole voids referred to as KH1. The Stock samples are processed at a volumetric energy density of 55.56 J/mm³ with a laser power of 280w, a scan speed of 1200 mm/s, hatch spacing of 140 $\mu m,$ and a layer height of 30 $\mu m.$ The KH1 set, designed to impart keyhole porosity but not substantially impact the microstructure, is generated at a volumetric energy density of 83.33 J/mm³ by lowering the scan speed to 800 mm/s. This introduces approximately 0.10% keyhole porosity as described in [29]. Samples are tested in the as-printed condition with no post-manufacturing heat treatment to maximize the influence of microstructure.

2.2. Mechanical testing

Tensile specimens with geometric dimensions shown in Fig. 1(a) are fabricated by laser powder bed fusion and then removed from the build plate via wire electric discharge machining (EDM). The samples are then tested on an electromechanical Instron 5984, using custom fixturing to interface with the self-aligning grip ends of the sample. All specimens are tested at a constant displacement rate of 8E-3 mm/s. The strain is measured using an Instron AVE2 non-contact video extensometer, with a gauge length of 8.5 mm.

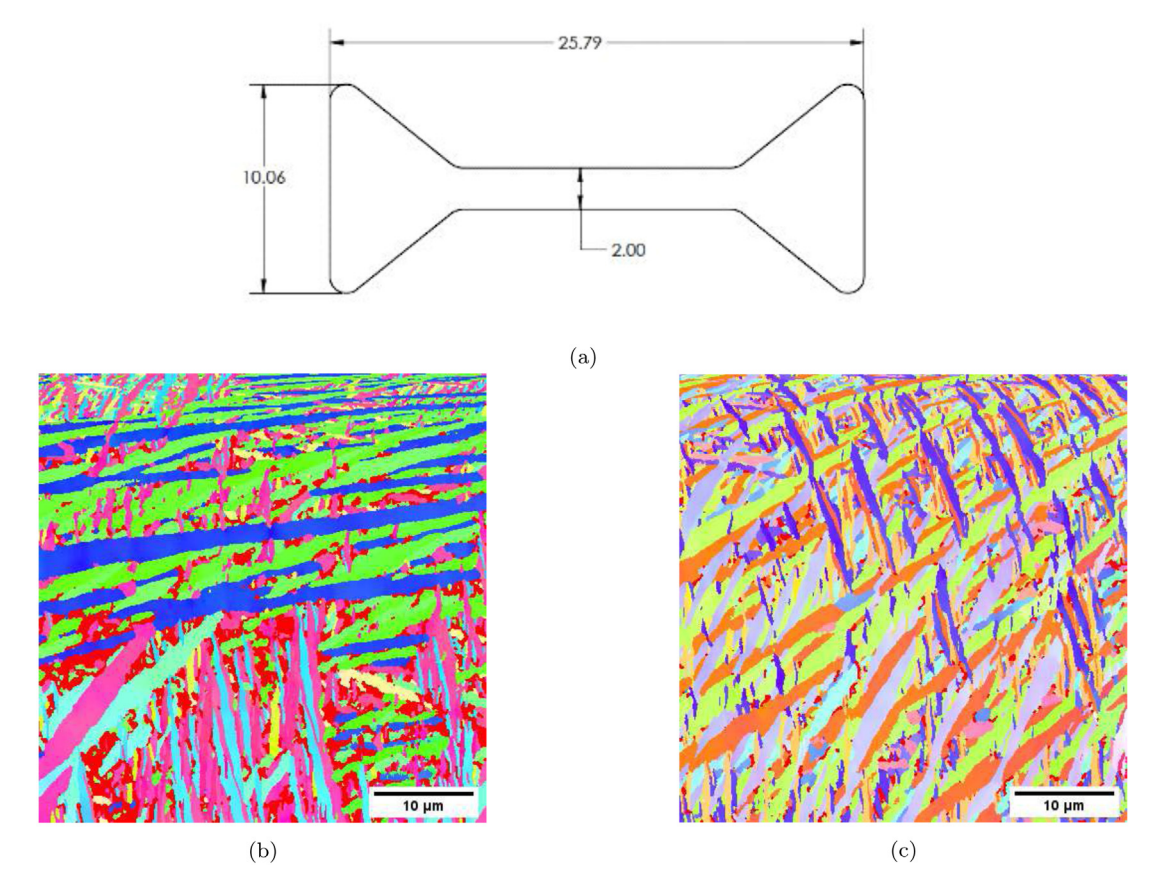


Fig. 1. (a) Geometry of the tensile specimen with dimensions in mm, (b) inverse pole figures (IPF) for the manufacturer recommended (Stock) build condition, and (c) IPF for the Keyhole 1 (KH1) build condition. The IPF keys are given in Fig. 2(d).

2.3. Imaging and data acquisition

The built samples are embedded in a slow-cure epoxy and ground with finer SiC paper. Subsequently, they are polished with a 1 μm alumina suspension. For acceptable surface finish of the EBSD scans, the samples are installed on a VibroMet $^{\text{TM}}$ 2 for approximately 17 h with 0.02 μm colloidal silica. EBSD scans are performed on a Thermo Scientific Scios scanning electron microscope equipped with an Oxford NordlysMax3 detector. An Oxford AZTEC data acquisition software is used to acquire and store the diffraction patterns at 100 nm or 1.2 μm resolutions, with an acceleration voltage of 25 kV. The high resolution 100 nm scans allow for the accurate identification of the individual α lath morphology. The lower-resolution 1.2 μm scans are able to capture a substantially larger area of the microstructure and are employed primarily to reconstruct the prior β microstructure. The Oxford Instruments Channel 5 software processes the raw EBSD data.

Following the ingestion of the raw EBSD data, an automated EBSD image cleanup and segmentation pipeline is established to obtain α lath morphological and crystallographic parameters at both scan resolutions. The high resolution, smaller area (200 $\mu m \times 200~\mu m$) scans in the XY plane are shown in Fig. 1, while the lower-resolution, larger area (3.6 mm \times 2.3 mm) scans contain information from both the XY and XZ planes. The figure shows gradients in the α lath dimensions, which is a consequence of significant thermal gradients and internal stresses during solidification [30,31]. With the micrographs shown in Fig. 2 imported into the microstructure builder DREAM.3D suite [32], the following image processing pipeline is applied to both the α and β images.

A bad data filter removes pixels that have a confidence index ≤
 0.1. Subsequently, a nearest neighbor fill approach is conducted for the bad data.

- 2. Contiguous grains with a 3° misorientation tolerance are identified.
- 3. A minimum size filter of 20 pixels is employed to eliminate imaging artifacts and over-segmentation of grain boundaries.
- The average crystallographic orientation and the best-fit ellipse are identified for every segmented grain, generating axis lengths and orientation.

The result of this pipeline is a fully segmented micrograph of α lath colonies, that contains statistical descriptors of each lath, viz. aspect ratio, orientation, axis lengths, equivalent sphere diameter, and crystallographic orientation.

2.4. Void characterization

The size and spatial distribution of voids are characterized by microfocus X-ray computed tomography (XCT). Representative cylindrical 6 mm diameter specimens, built under the stock and KH1 conditions, are volumetrically imaged with a voxel size of 6 μm . X-ray tomographs are acquired using a North Star Imaging X-50 system with a 225 keV X-ray source. Each specimen is scanned with the SubPix superresolution mode using 2401 projections and 2x frame averaging, while operating at 100 keV accelerating voltage and 130 μA source current. Each scan lasts about 53 min. Scans are subsequently reconstructed using the standard filtered back-projection algorithm implemented in the NorthStar Imaging reconstruction software.

The scans are post-processed using VolumeGraphics software VGStudioMax [33] to characterize the porosity. Pores are segmented using the EasyPore local thresholding algorithm, and pores smaller than 32 voxels (equivalent to a sphere with diameter of 24 μm) are excluded. The segmentation is manually inspected, and spurious pores due to ring artifacts are manually deleted. The location, volume, and diameter

of all pores in each volume are subsequently exported, which allows their size and spatial distribution statistics to be evaluated. Two distinct classes of non-densified defects are defined, viz. voids with a diameter greater than 24 μ m, and void volume fraction or porosity corresponding to those with a diameter less than 24 μ m. The former class is represented explicitly as voids in the microstructure of the micromechanical model, while the latter is represented as a porosity density or void volume fraction parameter in the crystal plasticity constitutive relation [25].

3. Generating statistically equivalent microstructural volume elements (SEMVE)

Statistically equivalent microstructural volume elements (SEMVEs) [34,35] are statistically optimal computational domains with respect to microstructural descriptors, used in the direct micromechanical simulations for evaluating material properties and local response variables. The SEMVEs of the AM-processed Ti-6Al-4V alloy represent ensembles of parent β grains, with α lath statistics manifested through parametric forms of representative ellipsoids in the accompanying crystal plasticity constitutive model. Details of this model have been given in [21]. Identical statistics are employed to generate different instantiations of the SEMVEs. Their volumes are taken to be sufficiently large such that random instantiations of the microstructure behave similarly, and deviations caused by random perturbations of unbiased statistical reconstructions are minimal. The α lath crystallographic orientations are determined from the parent β grain orientation by the Burgers relations.

The SEMVEs modeled has a length-scale that is of the same order as the test specimens, and hence their deformation modes can manifest non-homogeneity and non-periodicity such as necking. Correspondingly, it is not prudent to constrain the SEMVEs with periodic boundary conditions that do not accommodate inhomogeneous deformation. Conventional boundary conditions, such as displacement, periodicity, or traction boundary conditions can result in inaccuracies in the local state variables, particularly near the domain boundary [36]. A self-consistent boundary condition has been proposed in [26,27], where a concurrent multiscale domain as shown in Fig. 11(a) is constructed by embedding the SEMVE domain for crystal plasticity-based micromechanical simulations in an exterior domain modeled with self-consistent homogenized constitutive relations. A rate-dependent isotropic elastoplastic constitutive model is calibrated for the exterior domain in the concurrent model.

3.1. Identification of parent beta grains

During solidification in the LPBF process, the parent β grains with BCC lattice structure are formed with processing condition-dependent shape and orientations [37]. The α laths, with orientations following the Burgers relation, nucleate with cooling below the β transus temperature ~ 950°, and subsequently grow to cover the entire domain with further cooling. Alternative methods for reconstructing the parent β microstructure from observed α EBSD images have been proposed in [38,39]. A novel algorithm developed in [21] is used in this paper for the generation of β grain ensembles from microstructural α laths as shown in Fig. 2(a). This method first segments individual α laths into contiguous regions and lists all neighbors for each lath. For each neighboring lath-pair, a misorientation measure determines if these neighbors are derived from the same parent β grain, prior to being assigned to a common β grain candidate. This process is continued for all neighboring α lath-pairs for potential inclusion within a common β grain. Crystallographic orientation of the parent β grain candidate is calculated from those that share less than a threshold misorientation of 5°, and aggregated into a larger grain. Fig. 2(b) shows a representative β grain ensemble generated by this process.

3.2. Sampling volume fractions of variants

The statistical description of the α lath variant volume fractions is integral to the micromechanical crystal plasticity modeling of the additively manufactured Ti-6Al-4V SEMVEs [21]. The aggregated material response of the 12 variants is evaluated through a volume fraction-based weighted averaging. Hence, it is necessary to ensure unbiased sampling of the statistically equivalent sets of α lath variant volume fractions in the generation of SEMVEs.

For a given parent β grain, a 12-dimensional vector represents the volume fraction of its variants, with each dimension being the volume fraction of an individual variant. The construction of a 12-dimensional random variable with a large number of constraints would necessitate several assumptions on the relationship between the different dimensions. Instead of generating a probability density function (PDF) from which to sample, the approach used in this study matches critical cross-sections of the 12-dimensional PDF. Five necessary conditions are satisfied to ensure unbiased sampling with reasonable accuracy [21]. These are expressed as:

- 1. The number distribution of independent α variant volume fractions in the parent β grain must converge to the experimental distributions for a large sample, as seen in Fig. 3(a);
- 2. The volume fractions of all variants should add up to unity, i.e. $\sum_{i=1}^{12} v_f^i = 1$ for the entire parent β grain population;
- 3. The volume fraction distribution of α variants must converge to the experimental distribution for a large number of β grains, as in Fig. 3(b). This constraint is not placed on any one parent β grain, but on the population as a whole;
- 4. The total volume fraction distribution of each variant should closely match the experimental distribution, as shown in 3(c);
- 5. The pairwise correlation of α variant volume fractions calculated as: $c_{ij} = \sum_{k}^{N_{\beta}} \frac{v_{f_{k}}^{i} v_{f_{k}}^{j}}{v_{f}^{i} v_{f_{k}}^{j}} \ \forall \ i,j \in [1,12], \text{ as shown in 3(d), must be preserved.}$

A sampling method for generating statistically equivalent variant volume fractions has been described in [21]. For every β grain in the microstructure, the number N of different volume fractions is sampled from the experimental scan data. Next, N-1 points are randomly sampled from the [0,1] interval. The volume fraction assigned to the ith variant is defined by the distance between each of these points. Subsequently, the 12 variant IDs with assigned volume fractions are rearranged to satisfy the experimental variant ID distribution over all β grains. As shown in Fig. 3(d), the pairwise correlation c_{ij} between the variants is quite weak. The random sampling does not produce statistically significant correlations, and hence this needs to be accounted for

3.3. Alpha lath characterization and statistics acquisition

Generating SEMVEs of the 3D Widmanstätten microstructure is a challenging enterprise. Physics-based approaches to generating synthetic microstructures, e.g. the phase-field models [17–20] can be computationally expensive. Furthermore, the very high resolution needed to represent individual laths in the SEMVE makes their micromechanical analysis computationally intractable. To circumvent the overhead associated with explicit representation of large microstructural regions, the α lath statistics of the Widmanstätten microstructure are parametrically incorporated in the crystal plasticity constitutive model with underlying physics considerations. In this representation, the α laths are assumed to be adequately represented by ellipsoids, shown in Fig. 4, with parametric equations:

$$\left(\frac{\bar{x}}{A}\right)^2 + \left(\frac{\bar{y}}{B}\right)^2 + \left(\frac{\bar{z}}{C}\right)^2 = 1 \tag{1}$$

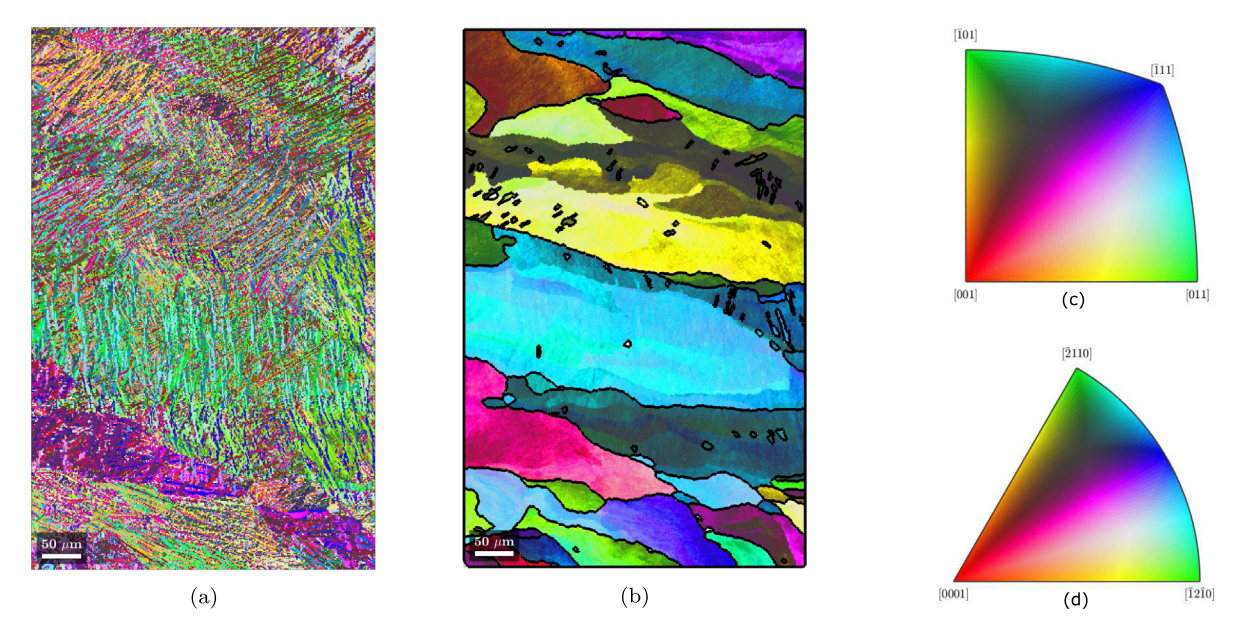


Fig. 2. (a) High resolution (1.2 μm) α lath image after preprocessing using steps in Section 2.2, (b) corresponding parent β grain ensemble constructed by an algorithm developed in [21], (c) inverse pole figure (IPF) key for the BCC parent β grains, and (d) IPF key for the HCP α grains images. The IPFs apply to all figures in this paper.

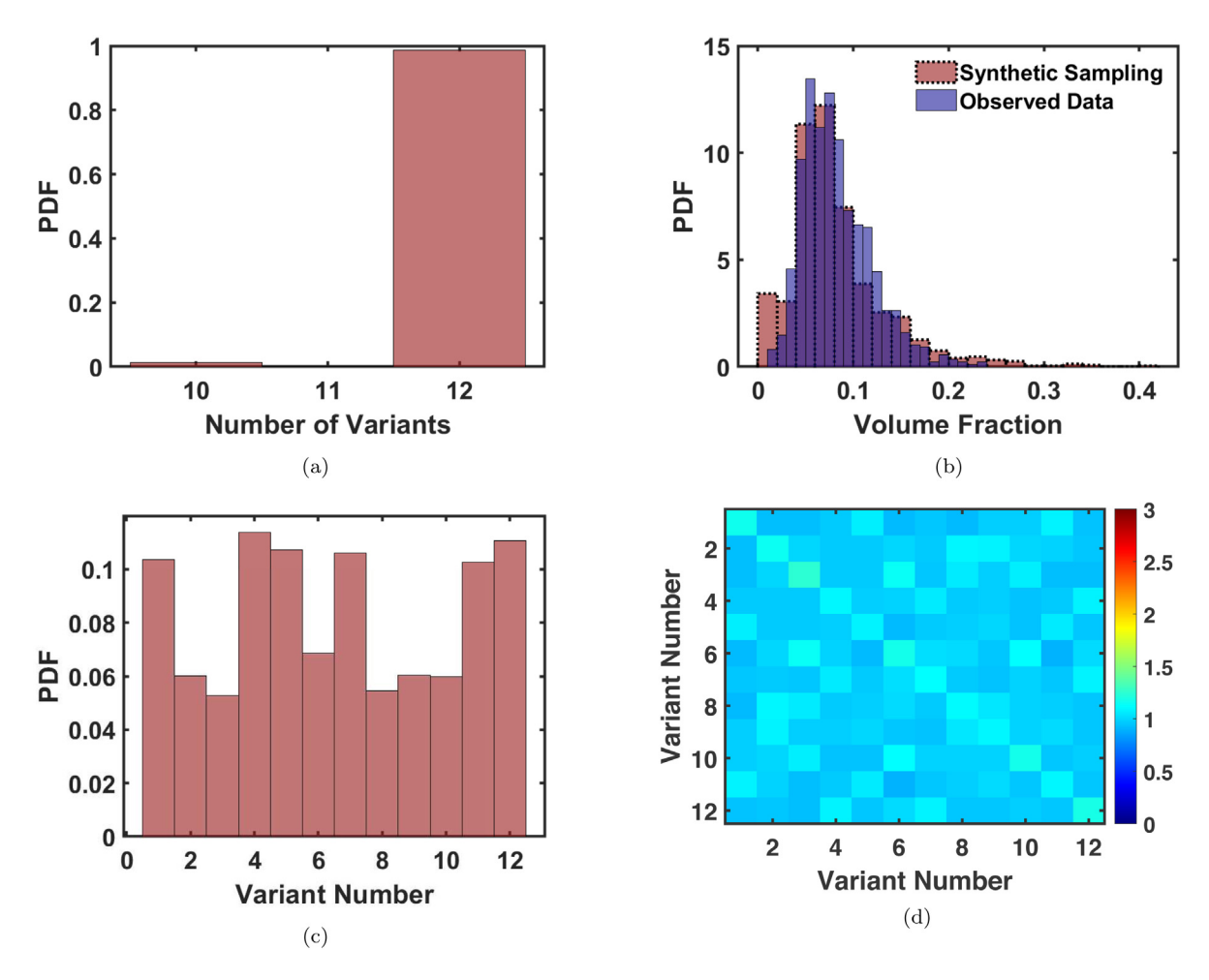


Fig. 3. (a) Histogram of PDF of the number of independent variants for each experimentally observed parent β grain, (b) comparison of the PDF of the average volume fraction in a parent β grain with that generated by the sampling method for a given variant, (c) histogram of PDF of the volume fraction for each of the 12 potential variants, and (d) pairwise correlation matrix c_{ij} of variant IDs relative to predicted values across all variants.

A,B,C are the semi-major, intermediate, and semi-minor axis lengths respectively, and \bar{x},\bar{y},\bar{z} are coordinates of a point on the surface in

a reference coordinate system with unit vectors $(\mathbf{e}_{\bar{\mathbf{x}}},\mathbf{e}_{\bar{\mathbf{y}}},\mathbf{e}_{\bar{\mathbf{z}}})$ along the ellipsoid axes, with its origin \mathbf{x}_0 at the centroid. The plane normal to

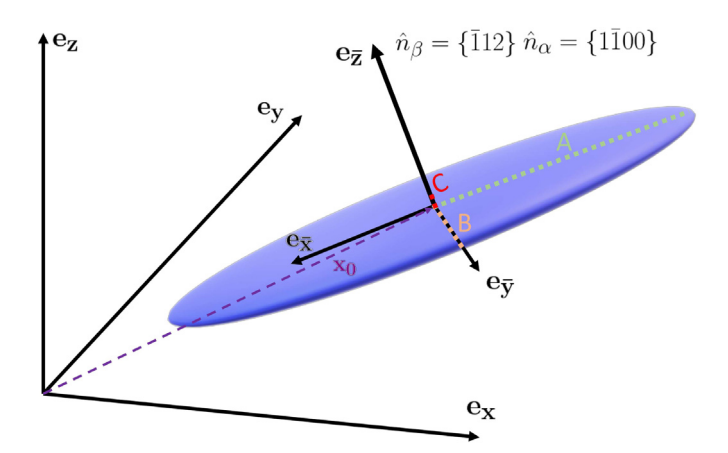


Fig. 4. The representative 3D α lath ellipsoid with its principal axes showing the relation between the \bar{z} axis direction \mathbf{n}_{α} and the β grain crystallographic direction \mathbf{n}_{β} .

 $\mathbf{e}_{\bar{\mathbf{z}}}$ is defined as the habit plane. As shown in Fig. 4, the minor $\bar{\mathbf{z}}$ axis direction \mathbf{n}_{α} and the β grain crystallographic direction \mathbf{n}_{β} follow the Burgers relationship $\{1\bar{1}00\} \parallel \{\bar{1}12\}$ [40].

The most probable 3D α lath ellipsoid is determined by a sampling process given in [21]. With known principal axis \bar{z} , the other two axes \bar{x} and \bar{y} are selected randomly about it. The most probable ellipsoid aspect ratios A/C and A/B are established by a sampling method in which 2D ellipses, extracted from the intersection of the 3D ellipsoid with a centroidal XY plane, best match the aspect ratios from EBSD scans. Subsequently, the ellipsoid size is estimated from the relation between principal axis lengths (A,B,C) and the semi-minor axis length of the 2D ellipse, resulting from the intersection of the most probable 3D ellipsoid with the XY plane.

For each segmented α lath, the corresponding variant ID \in [1 – 12] and β orientation are identified, and the normal to the habit plane is calculated. Next, about 50 ellipsoids are generated by sampling the aspect ratios A/B and A/C from the most probable distributions, and randomly selecting a rotation about the $e_{\bar{\tau}}$ axis that defines the $e_{\bar{\nu}}$ and $e_{\bar{x}}$ axis orientations. 2D projections of each randomly generated ellipsoid are taken through the centroid of the 3D ellipsoid on the imaging plane. Due to the uncertainty in calculating the orientation of the observed 2D ellipses, only the aspect ratios of the resultant 2D ellipses are used to determine the best-fit metric. Note that the absolute size of the ellipsoids can be scaled independently of the aspect ratio and orientation. The semi-minor axis length C is bounded by the smallest of 2D ellipse axis lengths measured in EBSD scans. For each β grain in the SEMVE, 12 statistically equivalent α laths are sampled and assigned to each variant. The characteristic ellipsoids ascribed to the variants are dispersed uniformly over the β grains, and hence they do not display spatial variation in the SEMVEs.

The 3D α lath generation results for the AM Ti-6Al-4V microstructures of the KH1 (with keyhole voids) and Stock samples are plotted in Figs. 5(a–c). The resultant A/C aspect ratio in Fig. 5(a) shows very little difference between the two samples. A log-normal distribution is chosen for parameterizing the distributions of all quantities with a reasonable fit. The difference between the samples is minimal for the overall minor (C) semi-axis length in Fig. 5(b). With similar statistics, the microstructure reconstruction process going forward uses the combined statistics from both the KH1 and Stock samples. The semi-axis lengths for these combined statistics along with their log-normal fit are plotted in Fig. 5(c).

3.4. Characterization and SEMVE reconstruction for the parent β grain

3D statistical representation of the parent β microstructure in the SEMVEs is necessary for micromechanical analysis. Building 3D virtual

microstructural images from image stack data generated by FIB-SEM-based serial sectioning methods [34,35] can be an extremely resource-intensive procedure. Alternatively, statistically equivalent 3D virtual microstructures have been developed from 2D orthogonal EBSD/SEM scans, whose 2D statistics in the orthogonal planes match the extracted images [10,41]. The approach in this paper for validating the 3D SEVMs of parent β grains incorporates the following modules: (i) generation of 3D virtual microstructures from a data set of 3D statistics, (ii) extraction of orthogonal slices from the reconstructed microstructure, (iii) comparison of the 2D statistics extracted from sections of the 3D microstructure to reference statistics from 2D experimental observations, and (iv) iterative enhancement of the 3D microstructure statistics.

The statistics of parent β grain morphology and crystallography are first extracted from orthogonal XY and XZ plane EBSD scans and processed using the DREAM.3D software [32], augmented with an in-house wrapper code. The DREAM.3D software uses an equivalent ellipsoidal grain generator to create pseudo-grains with size, shape, and orientation distributions equivalent to those in the experimental EBSD scans. This is followed by a constrained grain packer from spatial distribution statistics that places the generated pseudo-grains inside of a representative polycrystalline microstructural volume using a seed point generator and a constrained Voronoi tessellation method [42,43].

For the AM Ti-6Al-4V microstructures, contiguous parent β grains in the 2D EBSD images, obtained in Section 2.3 and depicted in Figs. 7(a,b), are segmented and parametrized as 2D ellipses in DREAM.3D. The distribution functions of three characteristic parameters of the ellipses, viz. (i) equivalent grain size represented by an equivalent sphere (circle) diameter (ESD), (ii) aspect ratio (AR), and (iii) an angle of rotation for the longest axis, are used as discriminating metrics to validate the equivalence of the experimental and reconstructed microstructures. The equivalent diameter is calculated as $ESD = 2\sqrt{\frac{A_s}{\pi}}$, where A_s corresponds to the 2D grain area observed in the EBSD scans. Its distribution is approximated by the log-normal distribution with mean μ_{ESD} and standard deviation σ_{ESD} . The 2D aspect ratio AR is fit to a normal distribution with mean μ_{AR} and standard deviation σ_{AR} . The distribution of the rotation angle of ellipses in the 2D section images is characterized through a PDF of the rotation angle $f(\theta)$ with an Epanechnikov kernel distribution [44], for which the kernel bandwidth is theoretically optimal for normal distributions. The distribution functions for ESD, AR and the orientation from the EBSD scans constitute a reference data set.

Additional assumptions are made in building the parent β grain virtual microstructures. The 3D ellipsoidal pseudo β grains are found to share a common set of Euler angles describing their spatial orientation. Their overall size distribution across all orientations is described by $-\frac{(ln(x)-\mu_{ESD})^2}{2}$

a log-normal distribution $f(x) = \frac{1}{x\sigma_{ESD}\sqrt{2\pi}}e^{-\frac{UMACY-\mu_{ESD}}{2\sigma_{ESD}^2}}$ with mean and standard deviation parameters μ_{ESD} and σ_{ESD} respectively. The 3D aspect ratios C/A and B/A are characterized by a β distribution, given as $f(x) = \frac{x^{\alpha-1}(1-x)^{\beta-1}\Gamma(a+b)}{\Gamma(a)\gamma(b)}$, where Γ is the gamma function and $a_{AB}, b_{AB}, a_{AC}, b_{AC}$ are parameters. The aspect ratios and size are found to be minimally correlated. With these assumptions, the parent β grain microstructure is parametrized by a set of parameter statistics S_{3D} with components: (i) the Euler angles (ϕ_1, Φ, ϕ_2) describing the orientation of the grains, (ii) the size distribution parameters $(\mu_{ESD}, \sigma_{ESD})$, and (iii) the aspect ratio distribution function parameters $(a_{AB}, b_{AB}, a_{AC}, b_{AC})$. The objective is to find an optimal set of statistical parameters S_{3D} that minimizes the goodness of fit metrics GOF_{rot} , GOF_{ESD} and GOF_{AR} described in Eq. (2). The goodness of fit GOF functions represent the difference between the statistics of the EBSD data and that from 2D sections of the reconstructed 3D microstructures, for the rotation angle (θ) , equivalent sphere diameter (ESD), and aspect ratio (AR). For a specific 3D microstructural instantiation, the

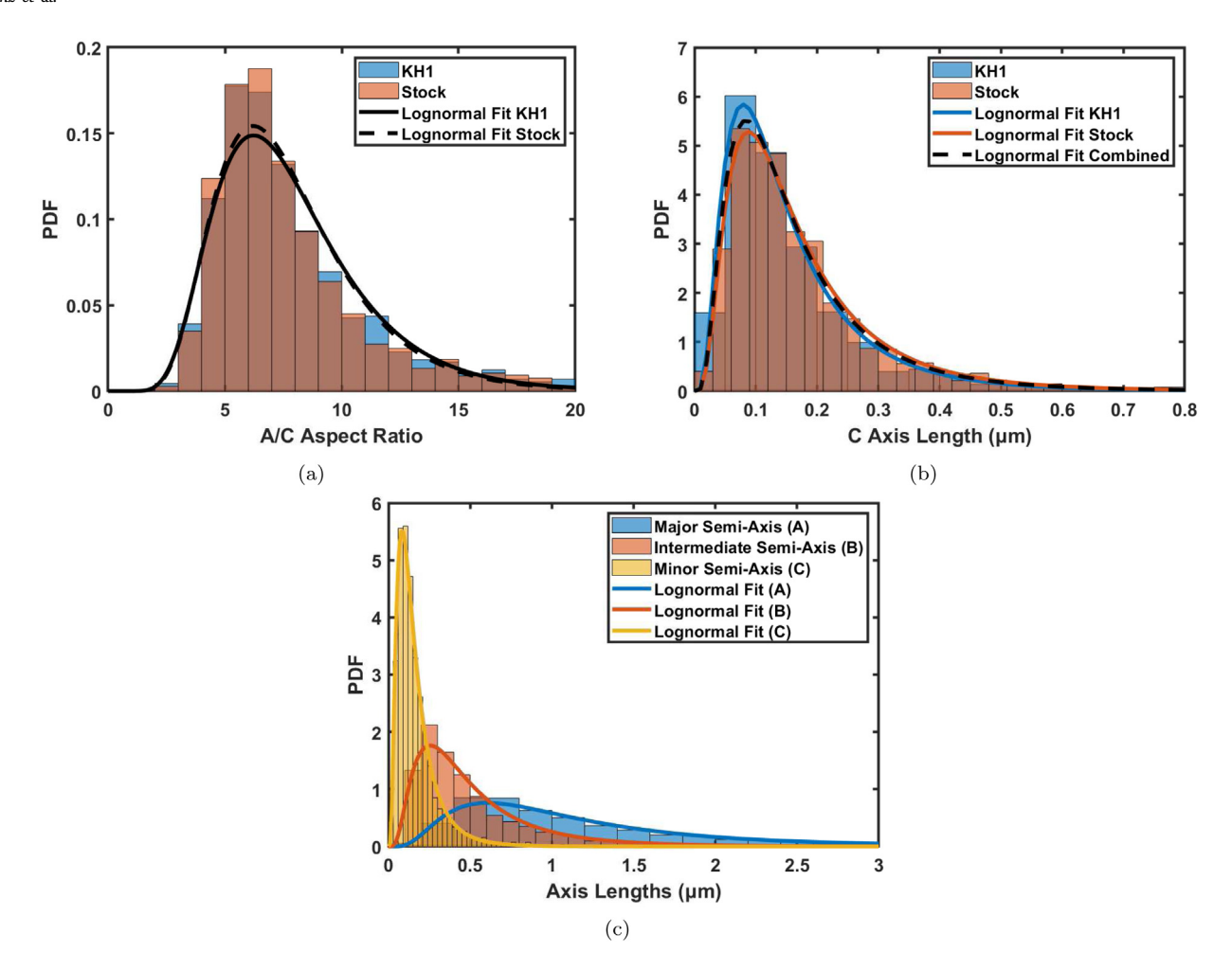


Fig. 5. (a) A/C aspect ratio of α laths for the AM Ti-6Al-4V microstructures of the KH1 (with keyhole voids) and Stock samples, (b) minor (C) semi-axis length distribution for the KH1 and Stock samples, along with their combined statistics, and (c) PDF of the semi-axis length distributions A, B, C.

functions are defined as:

$$\begin{split} GOF_{rot} &= \sum_{ndir}^{ndir} 1 - \int_{0}^{\pi} f^{sim}(\theta) f^{exp}(\theta) d\theta \\ GOF_{ESD} &= \sum_{ndir}^{ndir} 2(|\mu_{ESD}^{sim} - \mu_{ESD}^{exp}|) + |\sigma_{ESD}^{sim} - \sigma_{ESD}^{exp}| \\ GOF_{AR} &= \sum_{ndir}^{ndir} 2(|\mu_{AR}^{sim} - \mu_{AR}^{exp}|) + |\sigma_{AR}^{sim} - \sigma_{AR}^{exp}| \end{split} \tag{2}$$

where $1 \le ndir \le 3$ refers to the total number of orthogonal images available from experiments. The superscript sim corresponds to statistics of simulated microstructures, whereas superscript exp corresponds to those from the EBSD scans. The orientation direction is not explicitly specified in these equations. Statistics belonging to the same 2D plane are summed over all available directions. While the XY and XZ sections are accounted for in this work, the formulation is flexible to accommodate a third plane if available. The following steps are executed in the 3D SEMVE reconstruction.

- With initial estimates for the set S_{3D} (ϕ_1 , Φ , ϕ_2 , μ_{ESD} , σ_{ESD} , a_{AB} , b_{AB} , a_{AC} , b_{AC}), evaluated from 2D statistics in the EBSD scans, an initial 3D virtual microstructure is generated in DREAM.3D. A series of XY and XZ sections are digitally extracted from the 3D image at a 20 voxel spacing. A minimum cutoff size of 10 μ m is assumed for estimating β grains in each section. The PDFs of size, aspect ratio, and orientation of each section in the XY and XZ planes are then compiled as previously described.
- An iterative optimization scheme, implementing a Monte-Carlo type approach, sequentially minimizes the GOF metrics in Eq. (2)

for the aspect ratio, equivalent sphere diameter, and Euler angles. Upon calculation of GOF_{AR} for the initial 3D microstructure, the aspect ratio parameters in S_{3D} , i.e. $(a_{AB},b_{AB},a_{AC},b_{AC})$ are perturbed to create a trial set of 3D microstructural statistical parameters S_{3D}^{tr} using a method described in Appendix C. A new virtual microstructure is created in DREAM.3D using the set S_{3D}^{tr} and the corresponding GOF_{AR}^{tr} is evaluated. If $GOF_{AR}^{tr} \leq GOF_{AR}$, then the set is upgraded to $S_{3D} = S_{3D}^{tr}$, else S_{3D}^{tr} is discarded for a different trial set. The process is repeated for 30 iterations in this study.

- The next step entails the minimization of the goodness of fit metric GOF_{ESD} . The 3D virtual microstructure resulting from the previous step is sectioned, and 2D ESD statistics are extracted to generate GOF_{ESD} . A trial set of 3D microstructural statistics S_{3D}^{tr} is created with random sampling-based perturbed log-normal distribution parameters $\mu_{ESD}^{tr} = \mu_{ESD}(1+2up-p)$ and $\sigma_{ESD}^{tr} = \sigma_{ESD}(1+2vp-p)$, where p is a perturbation factor (taken as 0.1 in this study), and $u,v \in [0,1]$ are randomly generated parameters. The corresponding 3D microstructure, created in DREAM.3D, is sectioned and the metric GOF_{ESD}^{tr} is evaluated. The statistics set is upgraded to $S_{3D} = S_{3D}^{tr}$ only if $GOF_{ESD}^{tr} \leq GOF_{ESD}$. This loop is executed for 30 iterations in this study.
- The next minimization process is for the goodness of fit metric GOF_{rot} of the set S_{3D} containing 3D ellipsoidal grains with the orientation (Euler angles) represented by a rotation matrix R. Subsequent to the initial microstructure generation, sectioning and evaluation of GOF_{rot} , trial Euler angles are obtained by perturbing the existing set of Euler angles through a random

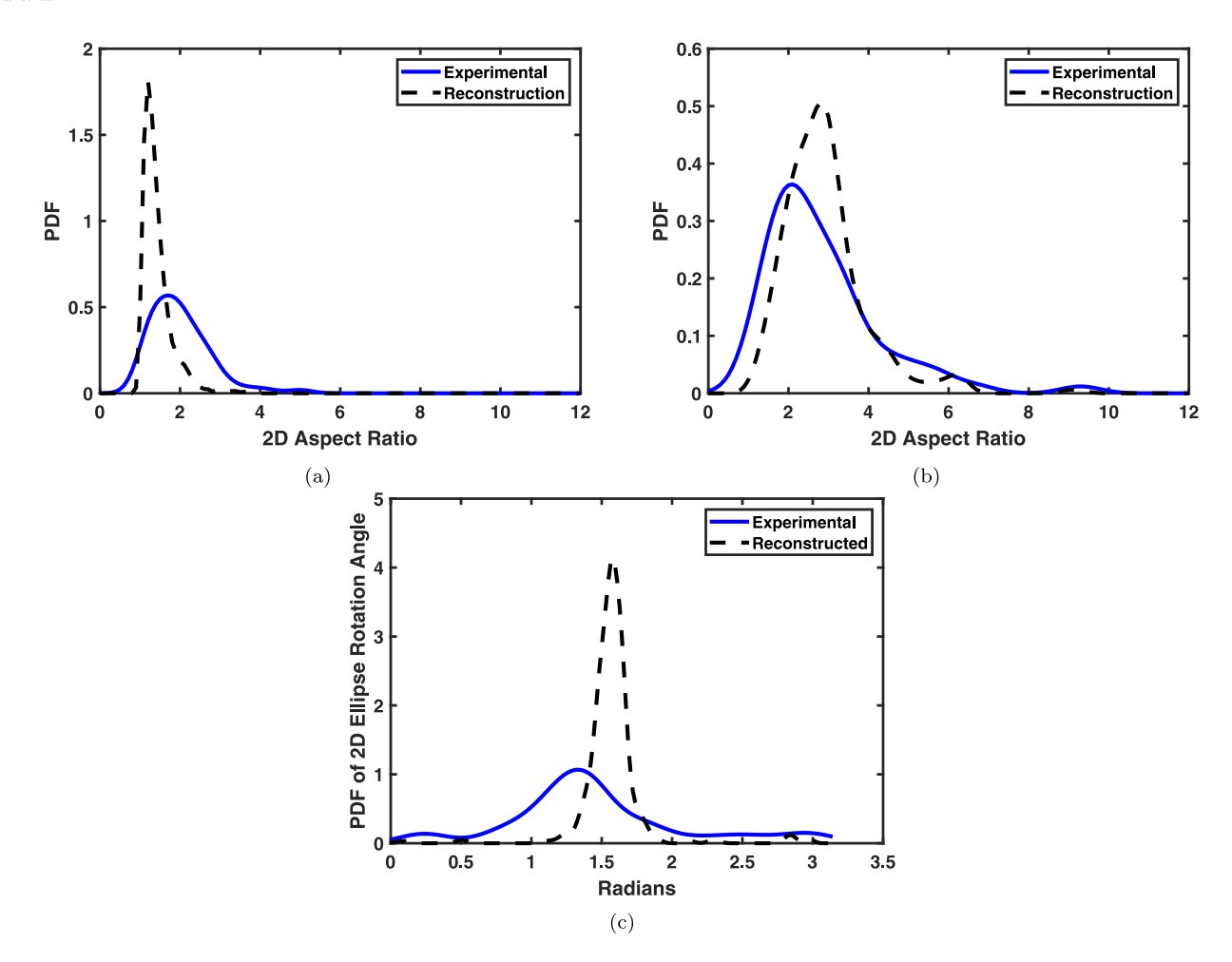


Fig. 6. Comparing the PDFs of the reconstructed pseudo-β grain sections and experimental EBSD scans: (a) aspect ratio in the XY plane, (b) aspect ratio in the XZ plane, and (c) Euler angle distribution in the XZ plane.

angle $\theta \in [0, \theta_{max}]$, where θ_{max} represents the maximum allowable perturbation in Euler angles. A rotation axis is chosen randomly from a unit sphere and the corresponding rotation matrix R_p representing a rotation about this axis by and angle θ is generated. The effective rotation matrix describing the orientation of the ellipsoids is expressed as $R^{tr} = R_p R$. The software package MTEX [45] is used to convert the rotation R^{tr} to an Euler angle representation, which is then included in the trial set S_{3D}^{tr} . As with the other metrics, the corresponding 3D microstructure created in DREAM.3D is sectioned and the metric GOF_{rot}^{tr} is evaluated. The statistics set is upgraded to $S_{3D} = S_{3D}^{tr}$ only if $GOF_{rot}^{tr} \leq GOF_{rot}$. This procedure is iterated for 15 iterations in this study.

 The individual optimization processes are executed within an outer iteration loop (8 in this study), to ensure convergence of the microstructural statistics.

The PDFs of aspect ratios in the XY and XY planes and the Euler angles representing the orientation of the equivalent ellipsoids for the reconstructed microstructures are compared with the experimental distributions in 6. The comparison is found to be reasonable, given the assumptions made in the reconstruction, e.g. the Euler angles for all grains in the microstructure are within a small tolerance with respect to each other, as well as the constraints imposed in the DREAM.3D software. Fig. 7(c,d) shows the XY and XZ grain section maps of the reconstructed parent β microstructure. The figures demonstrate that grains are elongated in the build direction, but relatively equiaxed in the XY plane. This is also seen in the PDF plots of the optimized equivalent sphere diameter and the aspect ratios in Figs. 8. For this data

set, it may be inferred that only the build direction has a discernible difference in the morphology, as the processing conditions in the other directions are similar.

4. Effective crystal plasticity model for parent β grains

An effective crystal plasticity model has been developed for parent β grains of AM-processed Ti-6Al-4V, with a parametric representation of α lath variant statistics in [21]. It accounts for the 12 α lath HCP slip systems [46,47], and porosity evolution of the smaller voids \leq 24 µm [25]. The microstructural models in this study use combined statistics from the KH1 and Stock samples due to their statistical similarity. This section summarizes the major equations in the crystal plasticity constitutive model from [21,25].

• Stress-Strain Relation:

$$\mathbf{M} = \mathbf{C}_{\rho} \hat{\mathbf{S}}, \quad \text{where} \quad \hat{\mathbf{S}} = \mathbb{C} \mathbf{E}_{\rho}$$
 (3)

where **M** is the Mandel stress, \mathbf{C}_e is the right Cauchy–Green tensor, \mathbf{E}_e is the Green–Lagrange strain tensor, $\hat{\mathbf{S}}$ is the second Piola–Kirchhoff stress in an intermediate configuration, and $\mathbb C$ is a fourth-order anisotropic elasticity tensor.

• Plastic Velocity Gradient Tensor for an α Lath Variant:

$$\mathbf{L}_{p} = \sum_{i}^{N_{SF}} (1 - w_{1}^{i} f) \sum_{\alpha}^{N_{slip}^{i}} \frac{\partial e_{*}^{\alpha}}{\partial \tau_{*}^{\alpha}} \frac{\partial \tau_{*}^{\alpha}}{\partial \mathbf{M}}$$
 (4)

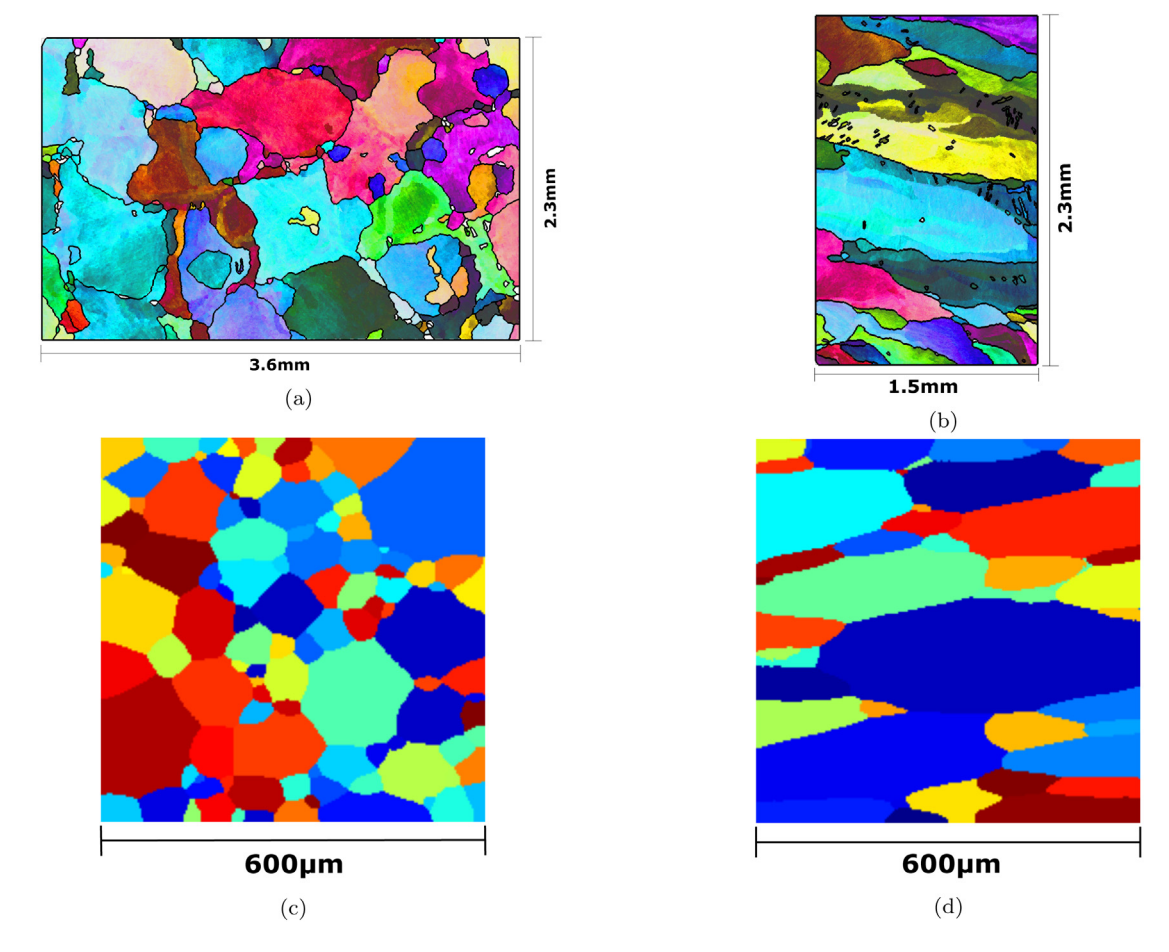


Fig. 7. Comparison of the experimental and reconstructed images of the parent β microstructure: (a) IPF of the XY plane EBSD image, (b) IPF of the XZ plane EBSD image, (c) XY grain section map of the reconstructure. The IPF keys for (a,b) are given in Fig. 2(c).

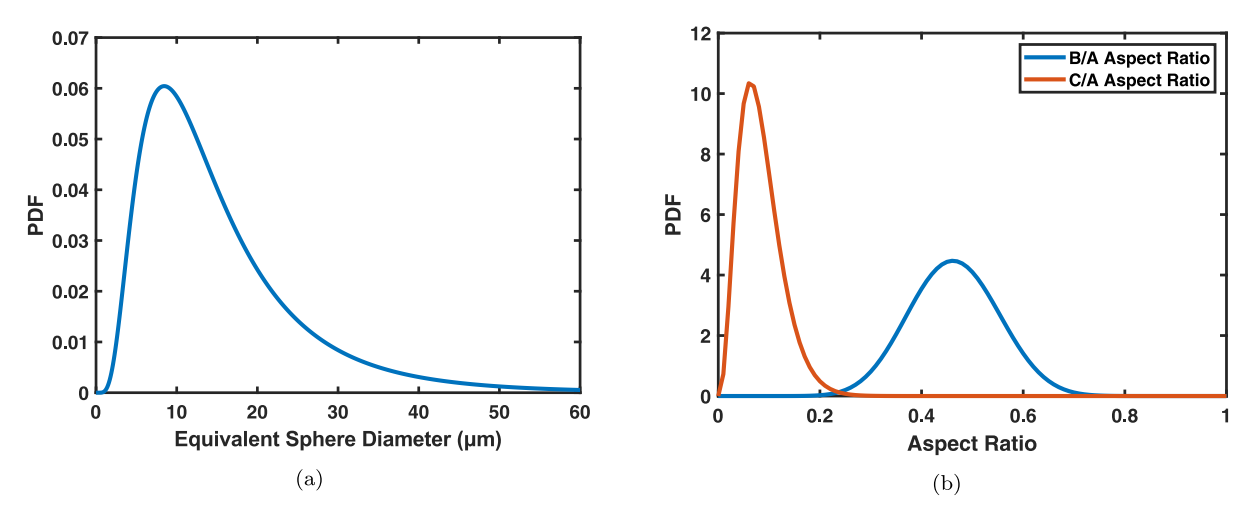


Fig. 8. PDFs of (a) the equivalent sphere diameter, and (b) the aspect ratios $\frac{B}{A}$ and $\frac{C}{A}$, of the reconstructed parent β grains.

where $e^{\alpha}_* = \frac{\dot{\gamma}^{\alpha}_0}{m+1} \left(\frac{r^{\alpha}_*}{\bar{g}^{\alpha}_0}\right)^{m+1}$ is an effective slip potential for each variant, f is the void volume fraction, w^i_1 is a weighting parameter, τ^{α}_* is the effective resolved shear stress, N_{SF} and N^i_{slip} are respectively the total number of slip families and number of slip systems in the i-th slip family. For HCP crystals $N_{SF}=5$ corresponding to the $\langle a \rangle$ -basal, $\langle a \rangle$ -prismatic, $\langle a \rangle$ -pyramidal, $\langle c+a \rangle$ pyramidal I, and $\langle c+a \rangle$ pyramidal II slip families. \bar{g}^{α}_0 is

the initial slip-system resistance, and $\dot{\gamma}^{\alpha}_0$ and m are the reference slip-rate and rate sensitivity exponent respectively.

• Void Volume Fraction Evolution:

$$\dot{f} = (1 - f) \operatorname{tr}(\mathbf{L}_p) \tag{5}$$

• Effective Resolved Shear Stress τ_{α}^* Equation:

$$\left(\frac{\tau^{\alpha}}{\tau_{*}^{\alpha}}\right)^{2} + w_{3}^{\alpha}w_{1}^{\alpha}f\frac{M_{eq}^{2}}{(\tau_{*}^{\alpha})^{2}} + 2fw_{1}^{\alpha}\cosh\left(w_{2}^{\alpha}\frac{M_{m}^{2}}{\tau_{*}^{\alpha}}\right) - 1 - (w_{1}^{\alpha}f)^{2} = 0 \tag{6}$$

where $M_m = -\frac{1}{3}Tr(\mathbf{M})$ and $M_{eq} = \sqrt{\frac{3}{2}M_{ij}M_{ij}}$ are respectively the hydrostatic and equivalent Mandel stress, $\tau_\alpha = \mathbf{M}$: s_0^α is the resolved shear stress on the α slip plane, and s_0^α is the Schmid tensor.

• Slip System Weighting Parameters (in Eqs. (4) and (6)):

$$w_k^{\alpha} = a_k^{\alpha} + b_k^{\alpha} \tanh\left(-d_k^{\alpha} \left(\frac{f - f_0}{f_0}\right)\right), \quad \text{for } \{k = 1, 2\}$$
 (7)

where constants a_k, b_k, d_k for each k and w_3^{α} have been calibrated in [21,25].

• Plastic Slip Rate for a Slip System α :

$$\dot{\gamma^{\alpha}} = \dot{\bar{\gamma}}^{\alpha} \left\langle \frac{\left| \tau_{*}^{\alpha} - \chi^{\alpha} \right| - \tau_{GP}^{\alpha}}{g^{\alpha} + \tau_{GF}^{\alpha}} \right\rangle^{\frac{1}{m}} \operatorname{sign} \left(\tau_{*}^{\alpha} - \chi^{\alpha} \right)$$
 (8)

where $\tilde{\gamma}^{\alpha}$ is a reference slip rate, m is a rate sensitivity exponent, χ^{α} is the back-stress, $\langle \rangle$ is the Macaulay bracket, τ^{α}_{GP} and τ^{α}_{GF} are resolved shear stress components contributing to the parallel and forest geometrically necessary dislocations (GNDs) respectively.

Slip System Resistance due to Statistically-Stored Dislocations (SSDs):

$$g^{\alpha}(\theta) = \bar{g}_{0}^{\alpha} + g_{HP}^{\alpha} - \hat{g}^{\alpha} \left(1 - \exp\left(\frac{\theta - \theta_{ref}^{\alpha}}{\hat{\theta}^{\alpha}}\right) \right)$$
 (9)

where \hat{g}^{α} , \bar{g}_{0}^{α} , θ_{ref}^{α} , and $\hat{\theta}^{\alpha}$ are temperature-dependent constants, which have been calibrated in [48]. In this study $\theta=298$ K corresponding to room temperature. $g_{HP}^{\alpha}=\frac{K}{\sqrt{D^{\alpha}}}$ is the hardening component contributing to the Hall–Petch effect, where K is a coefficient calibrated in [49] and $D^{\alpha}=$

 $\sqrt{A(\mathbf{e}_{\bar{x}}\cdot\mathbf{m}_0^\alpha)^2+B(\mathbf{e}_{\bar{y}}\cdot\mathbf{m}_0^\alpha)^2+C(\mathbf{e}_{\bar{z}}\cdot\mathbf{m}_0^\alpha)^2} \text{ is the dislocation mean free path along the slip direction } \mathbf{m}_0^\alpha \text{ across the ellipsoidal } \alpha \text{ lath delineated in Eq. (1). The evolution equations for the hardness } \dot{g}^\alpha(t) \text{ and back-stress } \dot{\chi}^\alpha \text{ have been given in [21,48].}$

 Hardening Stress Components due to Parallel and Forest GND Interactions:

$$\tau_{GP}^{\alpha}=c_{1}^{\alpha}G^{\alpha}b^{\alpha}\sqrt{\rho_{GP}^{\alpha}+\rho_{AP}^{\alpha}},\quad \tau_{GF}^{\alpha}=\frac{Q^{\alpha}}{c_{2}^{\alpha}b^{\alpha^{2}}}\sqrt{\rho_{GF}^{\alpha}+\rho_{AF}^{\alpha}} \qquad (10)$$

where ρ_{GP}^{α} and ρ_{GF}^{α} are GND densities parallel and normal to the slip plane α . They are calculated from the Nye tensor given as $\mathbf{\Lambda} = \nabla \times \mathbf{F}_p$ [48].

• GND Augmentation Accounting for the Absence of Explicit α Lath Boundaries: ρ_{AP}^{α} and ρ_{AF}^{α} in Eq. (10) are GND augmentation terms needed to compensate for the absence of explicit α lath boundaries in the equivalent parent β grain model. The augmented GND density is approximated from [50] as:

$$\rho_{GND}^{\alpha} = c_5 \frac{\gamma^{\alpha}}{b^{\alpha} D^{\alpha}} \tag{11}$$

where γ^{α} is the cumulative slip and b^{α} is the length of the Burgers vector on a given slip system. The corresponding parallel and forest augmented GNDs are given as:

$$\rho_{AF}^{\alpha} = \sum_{\beta}^{N} \chi_{AF}^{\alpha\beta} |\rho_{GND}^{\beta} \sin(n^{\alpha}, t^{\beta})| , \ \rho_{AP}^{\alpha} = \sum_{\beta}^{N} \chi_{AP}^{\alpha\beta} |\rho_{GND}^{\beta} \cos(n^{\alpha}, t^{\beta})|$$

 $\chi_{AF}^{\alpha\beta}$ is the interaction matrix between slip systems given in [48].

• Cauchy Stress Tensor for a Material Point:

$$\sigma = \sum_{k=1}^{12} v_f^{(k)} \sigma^{(k)} \tag{13}$$

where the *k*th variant stress is $\sigma^{(k)} = \frac{1}{\det \mathbf{F}^{(k)}} \mathbf{F}_e^{(k)}^{-T} \mathbf{M}^{(k)} \mathbf{F}_e^{(k)}^T$.

This effective crystal plasticity model is implemented in a FEM framework for very efficient CPFEM simulations.

4.1. Calibration of the effective crystal plasticity parameters

Various parameters in the crystal plasticity and porosity evolution models are taken from previous studies in [21,25,48,49]. Only the critical resolved shear stresses and the elastic constants are calibrated in this paper. The following calibrations are for the specific material modeled in this paper and may not be generalizable to other pedigrees of AMprocessed Ti-6Al-4V alloys. For calibration, 5 SEMVEs are generated as shown in Fig. 9 and meshed into \approx 115,000 3D TET4 elements using the meshing package Simmetrix [51]. Displacement boundary conditions representing a strain-rate of $10^{-3}~{\rm s}^{-1}$ are applied up to an engineering strain of $\epsilon_{final}=6\%$. For the calibration process, a percentage error in the strain energy for experiments and simulations is defined as:

$$\Phi(\bar{\sigma}_{exp}(\epsilon), \bar{\sigma}_{sim}(\epsilon)) = \frac{1}{max(\bar{\sigma}_{exp})\epsilon_{final}} \int_{0}^{\epsilon_{final}} |\bar{\sigma}_{exp}(\epsilon) - \bar{\sigma}_{sim}(\epsilon)| d\epsilon \qquad (14)$$

where $\bar{\sigma}_{exp}$ and $\bar{\sigma}_{sim}$ are respectively the experimental and simulated engineering stress components, computed from nodal forces in the loading direction. The calibrated parameters for a given tolerance is $\Phi(\bar{\sigma}_{exp}(\epsilon), \bar{\sigma}_{sim}(\epsilon)) \leq 0.0065$ are given in column 2 of Table 1. The results of the calibration process are given in Appendix A. The experimental and SEMVE simulation-based material responses are shown in Fig. 10. Since the experimental stress–strain response of the KH1 and Stock samples are similar, an average response is shown in this figure.

5. Homogenized rate dependent isotropic plasticity model (RDIPM) for self-consistent boundary conditions in the concurrent FE model

The morphological non-uniformity of the β grain SEMVEs necessitates the application of effective boundary conditions that do not over-constrain simulations as with periodicity boundary conditions. A self-consistent boundary condition has been developed in [27] to avert over-constraining the SEMVE problem. The boundary condition is applied through a concurrent model shown in Fig. 11, in which the SEMVE is embedded in an exterior domain modeled by self-consistent homogenized constitutive relations.

The exterior domain of the concurrent model is modeled by a rate-dependent isotropic plasticity model (RDIPM) with an associative flow rule that are summarized here. The plastic deformation gradient \mathbf{F}_p is decomposed into a symmetric part D_p and an antisymmetric part W_p representing plastic spin, which is assumed to be negligible [52]. A power-law type flow rule is expressed as:

$$L_p \approx D_p = D_0 \left(\frac{Y}{Y_0}\right)^{\frac{1}{m}} N \tag{15}$$

where D_0 is the reference slip rate, m is the rate sensitivity exponent, Y_0 is the flow stress, and N is the normal to the yield function Y, expressed as:

$$Y = ((|\lambda_1|)^a + (|\lambda_2|)^a + (|\lambda_3|)^a)^{1/a}$$
(16)

 λ_1 , λ_2 , and λ_3 are the principal values of the deviatoric part of the second Piola–Kirchhoff stress tensor **S** in the intermediate configuration, and the exponent a determines the shape of the yield surface. For an associative flow rule (15), the direction of the plastic strain-rate is given by:

$$N = \frac{\frac{\partial Y}{\partial S^{dev}}}{\left|\frac{\partial Y}{\partial S^{dev}}\right|} \tag{17}$$

The evolution of the flow stress Y_0 , is formulated by a modified Voce-type law [53], given as:

$$Y_0 = \bar{Y}_0 + \hat{\alpha}exp\left(\left(\frac{\bar{\epsilon}_p}{\hat{\beta}}\right)^{\Psi}\right) + \bar{H}\bar{\epsilon}_p \tag{18}$$

where \bar{Y}_0 is the initial yield stress, \bar{H} , $\hat{\rho}$, $\hat{\alpha}$, and ψ are parameters that describe the material hardening behavior, and $\bar{\epsilon}_p = \int_0^t \sqrt{\frac{2}{3} \bar{D}_p'} : \bar{D}_p' dt$ represents the effective plastic strain, \bar{D}_p' being the deviatoric part of \bar{D}_p .

Table 1The convergence Φ metric in Eq. (14) between (i) the experimental and SEMVE-CPFEM simulation results, (ii) the rate-dependent isotropic plasticity model (RDIPM) and SEMVE-CPFEM simulation results, and (iii) the RDIPM simulation and experiment results.

Convergence metric:	Experiment-SEMVE	RDIPM-SEMVE	RDIPM-Experiment
Φ	0.0064836	0.0044927	0.0092336

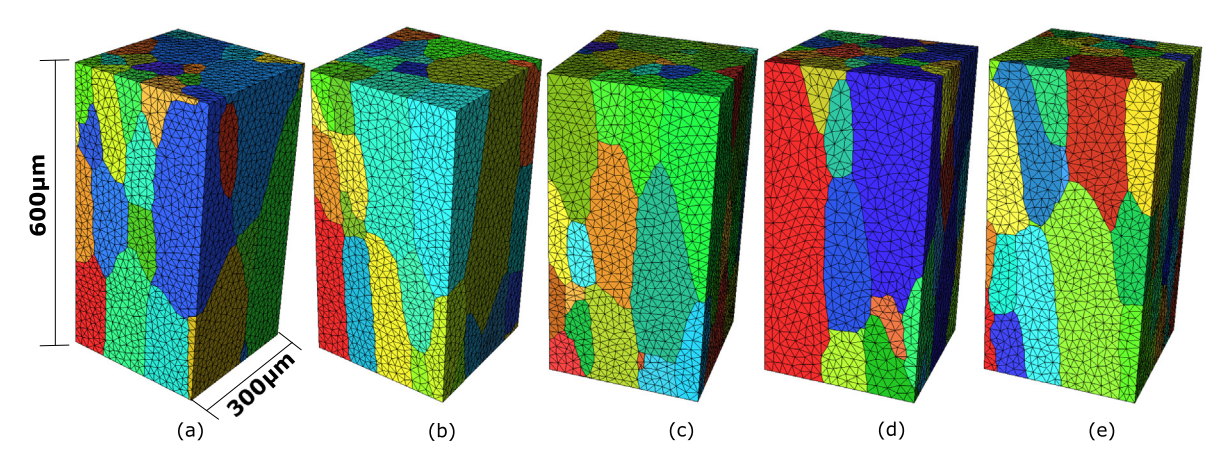


Fig. 9. Reconstructed parent β grain SEMVEs generated with 5 random initial conditions for calibration and prediction simulations. Colors represent individual grains in the ensemble. (For interpretation of the references to color in this figure legend, the reader is referred to the web version of this article.)

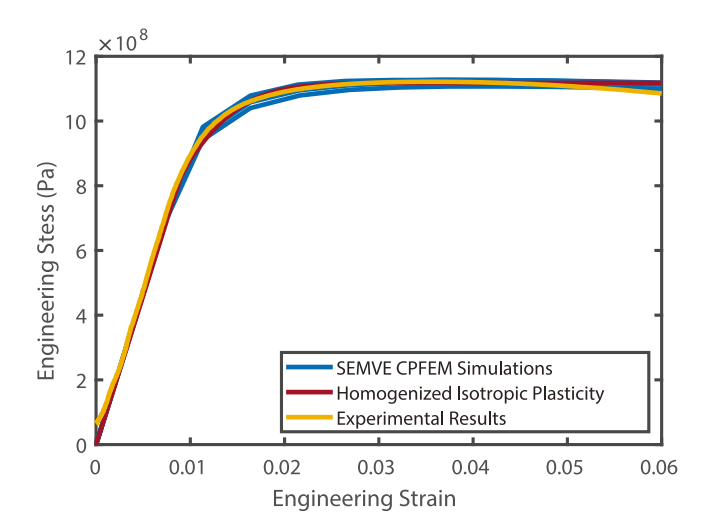


Fig. 10. Comparing engineering stress–strain curves from CPFEM simulation of the 5 SEMVEs with experimentally obtained response. The figure also shows the response predicted by the homogenized rate-dependent isotropic plasticity model.

5.1. Calibration of rate-dependent elasto-plastic isotropic plasticity parameters

The parameters \bar{Y}_0 , $\hat{\rho}$, \bar{H} , $\hat{\alpha}$, ψ of the rate-dependent isotropic plasticity model are calibrated from the volume-averaged engineering stress-engineering strain curve in Fig. 10 to achieve consistency in the behavior between the SEMVE and exterior domains. The results of the calibration process are given in Appendix B. The stress–strain response obtained by this self-consistent homogenized constitutive model is compared with the volume-averaged SEMVE and experimental responses in Fig. 10. Excellent convergence of the strain energy by this model to those by the SEMVE-CPFEM simulations and experiments are demonstrated in Table 1.

6. Simulations and parametric studies with the SEMVE model

Simulations with the SEMVE model are conducted using the self-consistent boundary conditions to avoid over-constraining with periodicity conditions, as explained in [27,36]. As shown in Fig. 11(a), this approach uses a concurrent model in which the SEMVE is embedded in a homogenized exterior material modeled by the rate-dependent isotropic plasticity model (RDIPM) developed in Section 5. The mesh in the exterior domain is graded from a fine resolution at the interface to a coarse resolution away from it for significant computational efficiency. Boundary conditions that mimic the experimental testing are applied to the boundary of the exterior domain. As demonstrated in Figs. 11(b,c), the self-consistent boundary condition facilitates continuity in the deformation and stress fields across the interface between the exterior and SEMVE domains. The set of 5 SEMVEs shown in Fig. 9 is simulated in this section to avoid a particular microstructural bias in the results.

6.1. Parametric study with explicit representation of voids in the SEMVE

A parametric study is conducted in this section for the effect of larger keyhole (KH) and lack of fusion (LOF) voids in the microstructure. To represent these voids, spherical (representing KH) and ellipsoidal (representing LOF) voids are explicitly inserted into the SEMVE models as shown in Fig. 12. While these are only approximate representations of the void morphologies, they provide a means of parametric representation with a relatively small number of parameters. The study in this paper gives a preliminary understanding of the effect of these void morphologies on the local stress fields, which can eventually influence microstructural damage. An important observation from the experimental CT analysis is that the voids have no radial spatial relationship to one another. This is shown with the radial distribution function g(r) in Fig. 11(d), which corresponds to the probability that the centroids of a pair of voids are at a distance r apart. The figure shows the experimental $g(r)^{exp}$, and two test distributions viz. a random distribution $g(r)^{rand}$ (where voids can overlap one another), and a hard sphere distribution $g(r)^{HS}$ (where random voids have a no penetration condition). Excellent agreement is seen between the experimental and the hard sphere distributions, which demonstrates that the spatial placement of the voids in space are random with respect to the radial dimension.

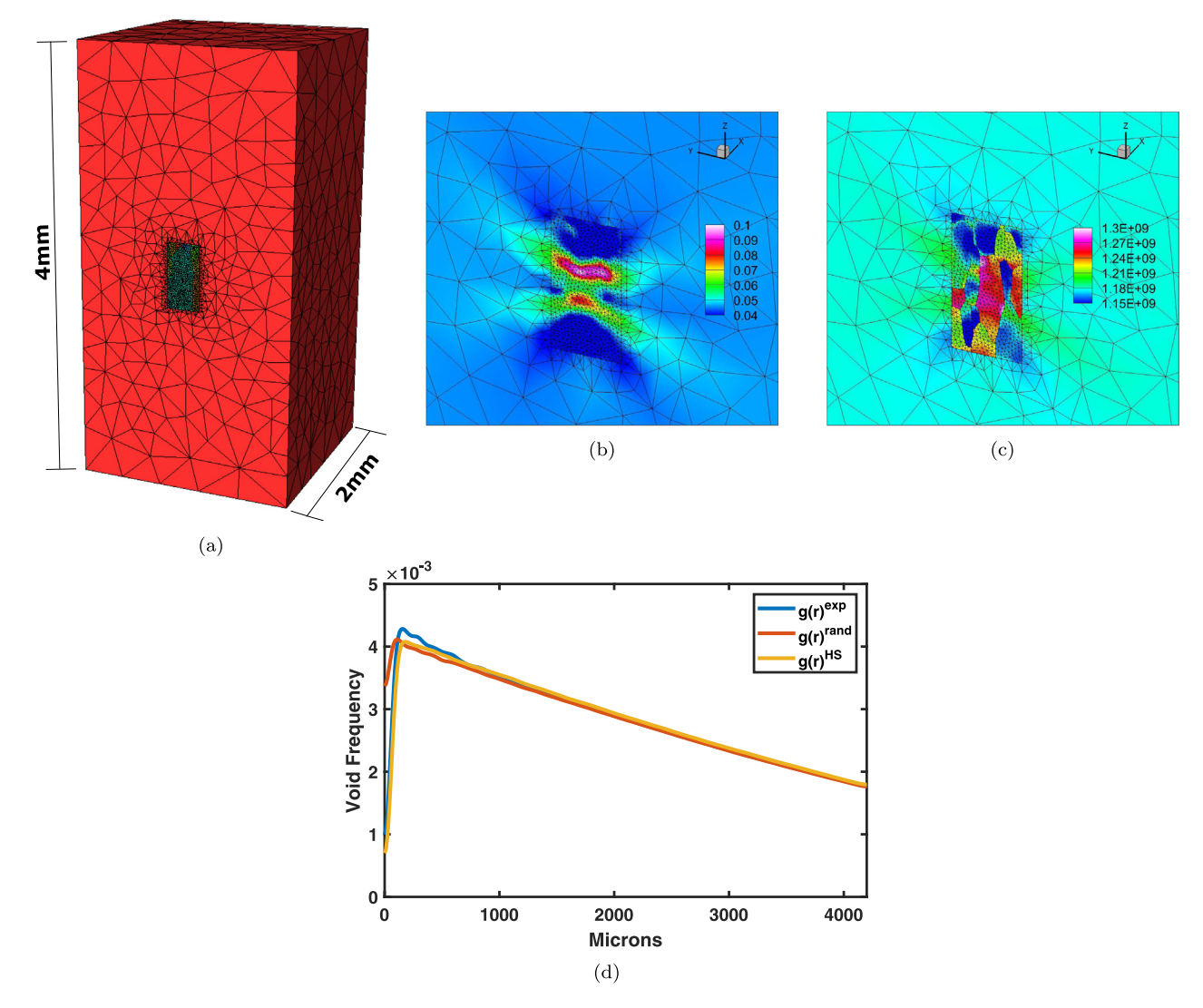


Fig. 11. Parent β SEMVE simulations with the self-consistent boundary conditions: (a) the concurrent model and mesh with the SEMVE embedded in an exterior domain modeled by the RDIPM, (b) equivalent plastic strain field, (c) Von-Mises stress in the concurrent model, exhibiting continuity in the fields across the interface, and (d) radial distribution functions $g(r)^{exp}$, $g(r)^{rand}$, and $g(r)^{HS}$ with Epanechnikov smoothing.

Table 2 Void characteristics for each of the 8 morphology cases. The aspect ratios correspond to $(\frac{A}{C}, \frac{B}{C}, 1)$ where $A \ge B \ge C$ are the principal axis lengths and Euler angles correspond to their orientations.

Morphology case	Void type	Aspect ratios	Volume fraction (%)	Euler angles
1	None	N/A	0%	N/A
2	KH	N/A	1%	N/A
3	KH	N/A	5%	N/A
4	LOF	8,4,1	1%	$\pi/2, 0, 0$
5	LOF	8,4,1	1%	$\pi, \pi/2, 3\pi/2$
6	LOF	8,4,1	1%	$\pi, \pi/4, 3\pi/4$
7	LOF	2,1.5,1	1%	$\pi/2, 0, 0$
8	LOF	6,3,1	1%	$\pi/2, 0, 0$

For this study, 8 different void morphologies, described in Table 2, are placed within each of the 5 SEMVEs in the concurrent model of Fig. 11(a). This corresponds to a total of 40 simulations for the 8 cases. Minimum boundary conditions are applied to the exterior domain boundary, while the material is loaded up to 6% engineering strain at a strain-rate of 10^{-3} s⁻¹. The initial void volume fraction for the crystal plasticity model is taken as f=0.11%. The parametric study identifies the morphological characteristics that have the most influence on the material response.

Three state variables, viz. the equivalent plastic strain (EPS), the Von-Mises stress (VM), and the loading direction Cauchy stress component σ_{zz} (LC), are studied in this example. For each of these state variables, the PDFs for each of the morphology cases are aggregated from simulations of the 5 SEMVE instantiations in Fig. 9. The metrics chosen to represent the response of these PDFs are the mean (μ^{EPS} , μ^{VM} , μ^{LC}), standard deviation (σ^{EPS} , σ^{VM} , σ^{LC}), and value at the 99th percentile of the distribution ($F(0.99)^{EPS}$, $F(0.99)^{VM}$, $F(0.99)^{LC}$). This last metric is chosen to represent the extreme values of the

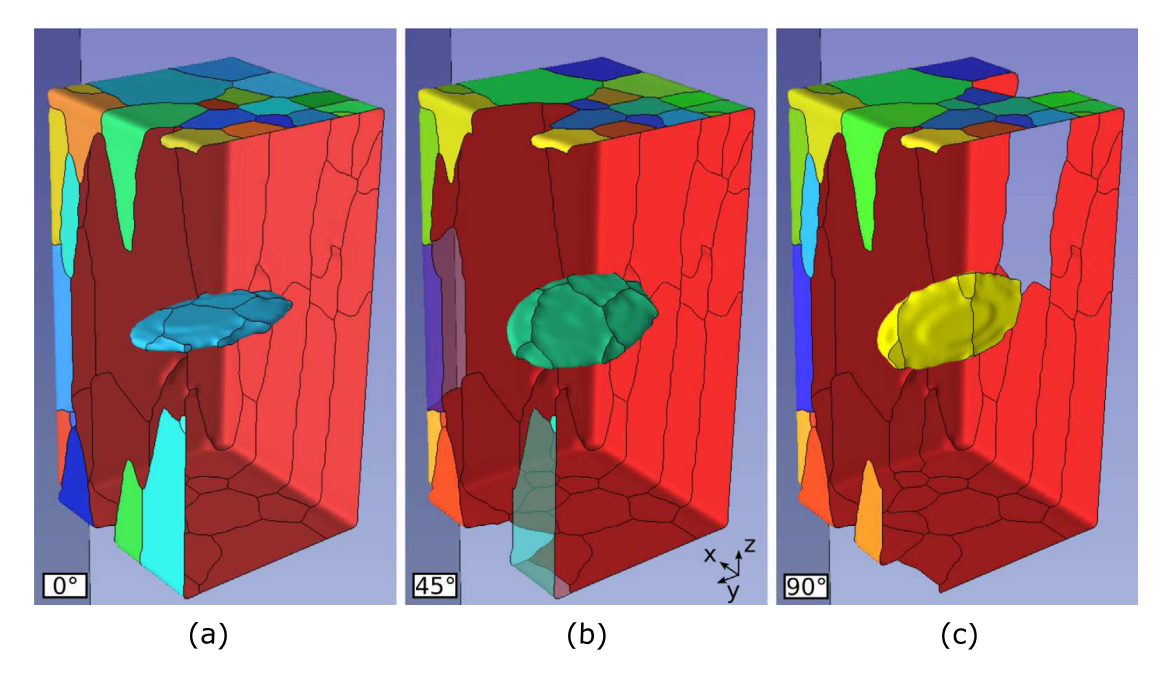


Fig. 12. Schematic of voids embedded in the SEMVE region of the concurrent model for (a) LOF void represented by case 4, (b) LOF void represented by case 5, and (c) LOF void represented by case 4 in Table 2. The colors represent different grains. (For interpretation of the references to color in this figure legend, the reader is referred to the web version of this article.)

Table 3 Scaled mean, standard deviation, and extreme value of the aggregated equivalent plastic strain, Von-Mises stress, and σ_{zz} for SEMVEs with spherical voids of 1% and 5% volume fraction.

	Keyhole 1%	Keyhole 5%
$\bar{\mu}^{EPS}$	0.99257	1.0086
$\bar{\sigma}^{EPS}$	5.8139	7.7067
$\bar{F}(0.99)^{EPS}$	1.679	2.0704
$\bar{\mu}^{VM}$	0.99776	0.99469
$ar{\sigma}^{VM}$	1.111	1.2663
$\bar{F}(0.99)^{VM}$	0.99935	0.99741
$\bar{\mu}^{LC}$	0.98081	0.95751
$ar{\sigma}^{LC}$	2.1582	2.7465
$\bar{F}(0.99)^{LC}$	1.0788	1.1434

response that are most likely to lead to material failure. The metrics are scaled by the values from simulations of the morphology case 1 (no voids), i.e. $\bar{\mu}_i^{EPS/VM/LC} = \frac{\mu_i^{EPS/VM/LC}}{\mu_i^{EPS/VM/LC}}, \ \bar{\sigma}_i^{EPS/VM/LC} = \frac{\sigma_i^{EPS/VM/LC}}{\sigma_i^{EPS/VM/LC}},$ and $\bar{F}(0.99)_i^{EPS/VM/LC} = \frac{F(0.99)_i^{EPS/VM/LC}}{F(0.99)_i^{EPS/VM/LC}},$ to yield a relative measure of response.

6.1.1. Effect of volume fraction

The effect of the void volume fraction on the state variables is determined by comparing the morphology cases 1, 2, and 3 in Table 2. Each of the cases embeds a void in the 5 SEMVEs of Fig. 9, as shown in Fig. 12. The PDFs of the equivalent plastic strain, Von-Mises stress, and σ_{zz} are aggregated for simulations of the 5 SEMVEs containing the voids and plotted in Fig. 13(a–c) respectively. The values of the scaled metrics are given in Table 3.

A comparison of the scaled results for 1% and 5% void volume fraction in Table 3 infers that an increase in the void volume does not significantly affect the mean of the equivalent plastic strain PDF. However, the standard deviation increases by a factor of 5.8 from 0 to 1% void volume fraction, and by a factor of 7.7 from 0 to 5% void volume fraction. Similarly, there is an increase by a factor of 1.67 and 2.07 in the 99th percentile strain for the 1% and 5% cases respectively, which corresponds to a substantial localized deformation.

Fig. 13(a) shows that increasing void volume fraction leads to a bimodal distribution in the PDF of the equivalent plastic strain. For the Von-Mises stress, the mean or the 99th percentile does not change much with increasing void volume fraction. However, the standard deviation is considerably larger with increased volume fraction. This is also observed in Fig. 13(b). For the loading direction stress σ_{zz} the mean decreases with increasing volume fraction indicating stress redistribution to the surrounding homogenized region. An increase in the standard deviation and extreme value is also seen as corroborated in Fig. 13(c).

6.1.2. Effect of aspect ratio

The effect of aspect ratio on the state variables is determined by comparing the cases 2, 4, 8, and 9 in Table 2. Again each case embeds a void in the 5 SEMVEs as shown in Fig. 12. The voids are oriented with the shortest axis parallel to the loading direction, and the total volume fraction considered for this study is 1%. The voids correspond to (i) *long* ellipsoid with an aspect ratio =8 (case 4), (ii) the *intermediate* ellipsoid with an aspect ratio =6 (case 8), (iii) *short* ellipsoid with an aspect ratio =2 (case 7), and (iv) sphere (case 2). The other aspect ratios are given in Table 2. The aggregated PDFs of the equivalent plastic strain, Von-Mises stress, and loading direction σ_{zz} are shown in Figs. 14(a–c) respectively. The scaled metrics are given in Table 4.

The void aspect ratio has a considerable effect on the mean, standard deviation, and extreme values of the PDF of the equivalent plastic strain, as seen in Fig. 14(a). With increasing aspect ratio, the distribution stabilizes with larger moments. This results in a lower mean, but higher values of both the standard deviation and the extreme values. The Von-Mises stress and σ_{33} have less pronounced effects, but the overall trends are similar to that of the equivalent plastic strain.

6.1.3. Effect of orientation

Finally, the effect of void orientation on the state variables is assessed from the morphology cases 4, 5, and 6 in Table 2. The void in case 4 is oriented such that the shortest axis is parallel to the loading direction z, and the longest axis parallel to the y direction, as shown in Fig. 12(a). For case 5, the void is oriented such that the intermediate and the shortest axis are both at 45° to the loading (z) axis as shown in Fig. 12(b), while for case 6 the intermediate axis is parallel

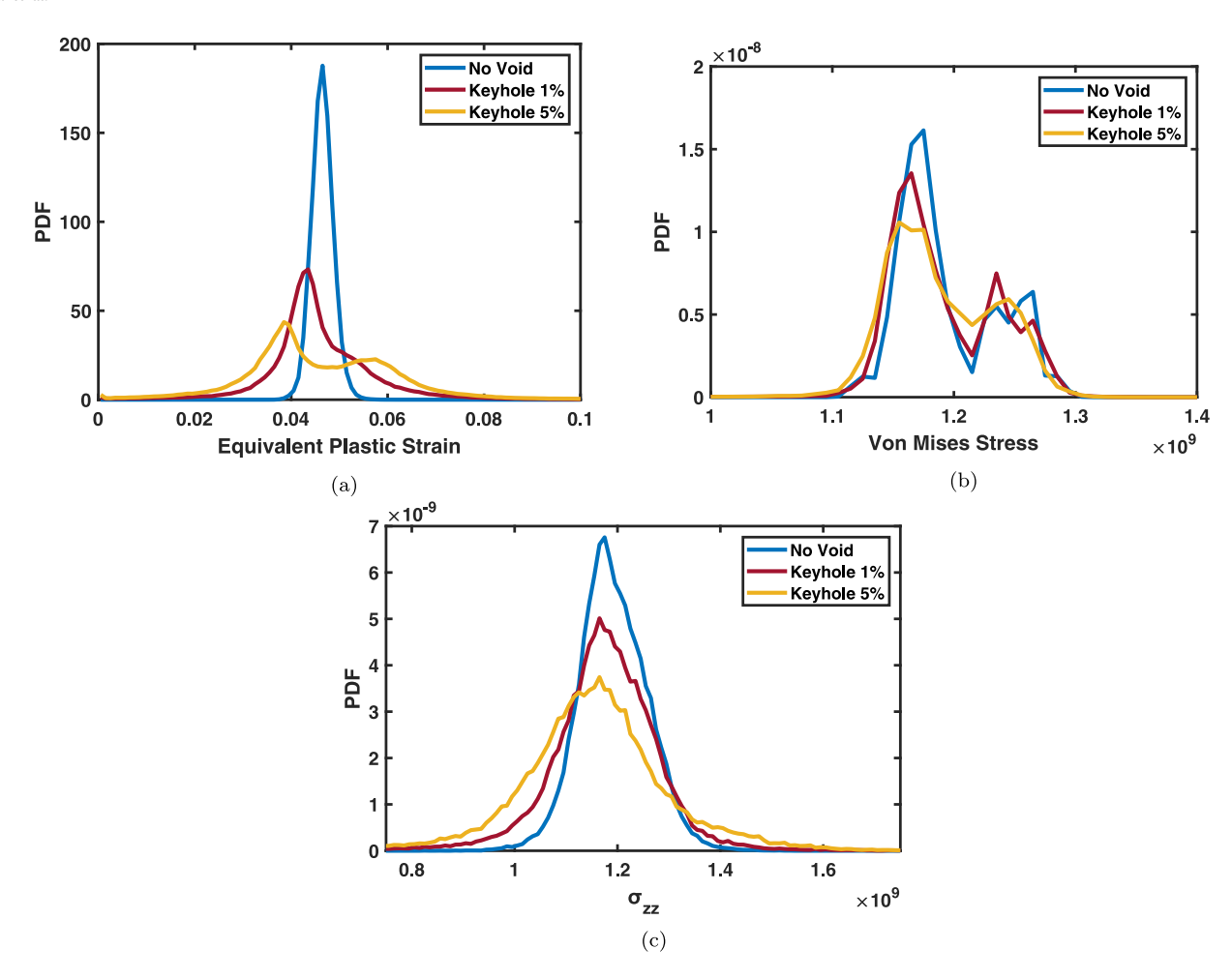


Fig. 13. The aggregated PDFs (over 5 instantiations) of (a) the equivalent plastic strain, (b) Von-Mises stress, and (c) and σ_{zz} for the SEMVEs containing 0%, 1% and 5% void volume fractions.

Table 4 Scaled mean, standard deviation, and extreme value of the aggregated equivalent plastic strain, Von-Mises stress, and σ_{zz} for SEMVEs with (i) long ellipsoid void (case 4), (ii) intermediate ellipsoid void (case 8), (iii) short ellipsoid void (case 7), and (iv) sphere (case 2), all with 1% void volume fraction.

	Long ellipsoid	Intermediate ellipsoid	Short ellipsoid	Sphere
$\bar{\mu}^{EPS}$	0.97802	0.991	0.99631	0.99257
$\bar{\sigma}^{EPS}$	10.8326	6.5563	4.5247	5.8139
$\bar{F}(0.99)^{EPS}$	2.4558	1.7896	1.4691	1.679
$\bar{\mu}^{VM}$	0.9955	0.99481	0.99706	0.99776
$\bar{\sigma}^{VM}$	1.2186	1.0868	1.0531	1.111
$\bar{F}(0.99)^{VM}$	1.0179	1.0046	1.0011	0.99935
$\bar{\mu}^{LC}$	0.95141	0.97081	0.98262	0.98081
$\bar{\sigma}^{LC}$	3.0904	2.3701	1.9882	2.1582
$\bar{F}(0.99)^{LC}$	1.2016	1.1203	1.0762	1.0788

to the loading (z) direction as shown in Fig. 12(c). The PDFs of the equivalent plastic strain, Von-Mises stress, and σ_{zz} are aggregated for the 5 SEMVEs and shown in Fig. 15(a–c). and the values of the scaled metrics are given in Table 5.

The orientation of the void relative to the SEMVE has a considerable effect on the mean, standard deviation, and extreme values of the PDF of the equivalent plastic strain, as seen in Fig. 15(a). Analogous to the aspect ratio, as the cross-sectional area of the void with respect to the loading direction increases, the mean of the EPS decreases, and the standard deviation and extreme values increase. These patterns are similar for the Von-Mises stress metrics and σ_{33} as shown in Figs. 15(b,c). However, the results are significantly less pronounced.

6.1.4. Discussion of results in this analysis

While the volume fraction, aspect ratios, and orientation of voids individually provide information on the effect on the distribution of state variables, more insights may be obtained from the projected cross-sectional area of the void normal to loading direction. Linear regression curves of $\bar{\sigma}^{EPS}$ and $\bar{F}(0.99)^{EPS}$ are generated for each case and the corresponding coefficient of determination R^2 values are computed as shown in Figs. 16. For both the standard deviation and the 99th percentile metrics, about \approx 85% of the variation between samples is due to the difference in the cross-sectional area, which is a major determinant of the material response. This analysis demonstrates that for the same volume fraction, spherical voids have a significantly lower

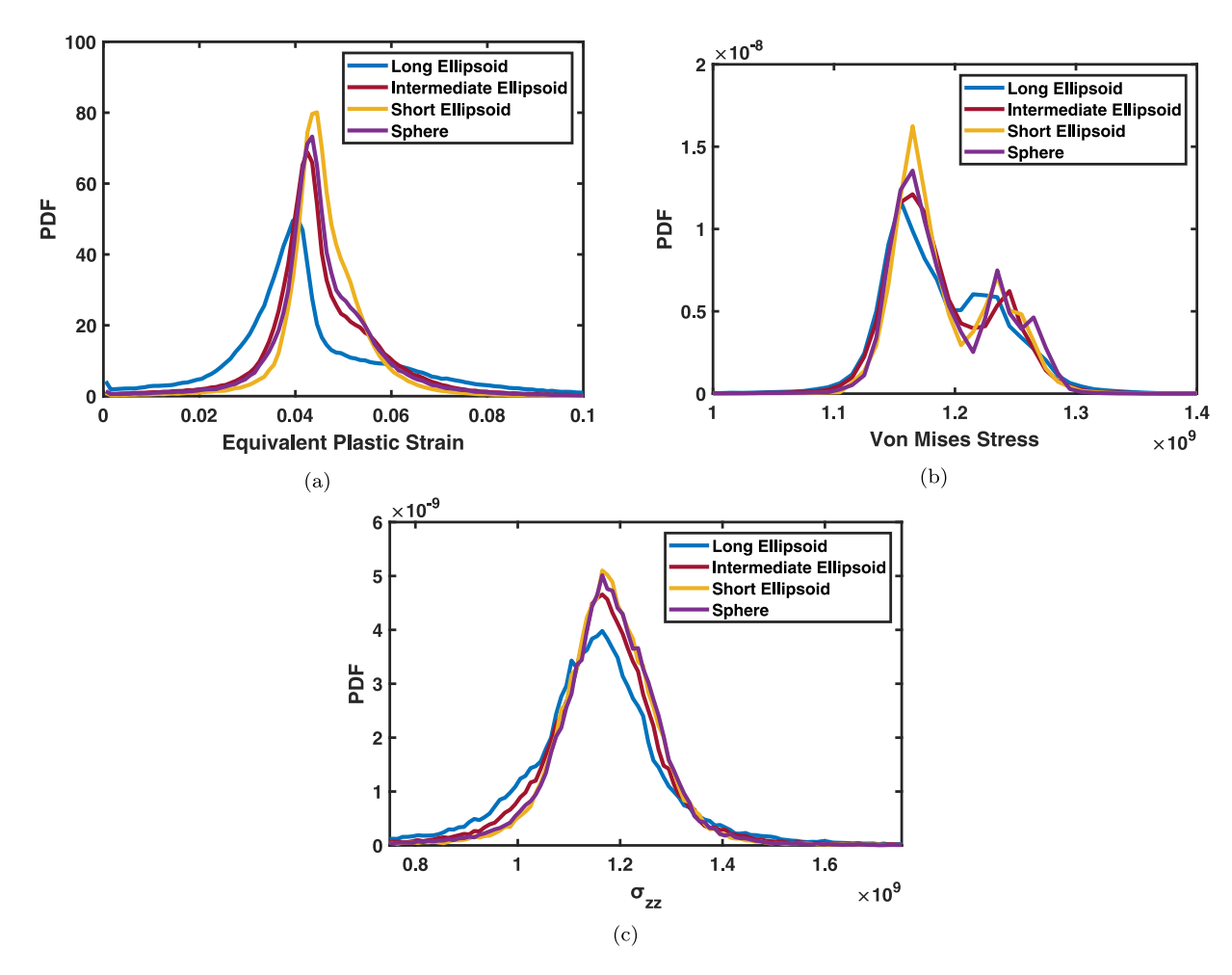


Fig. 14. The aggregated PDFs (over 5 instantiations) of (a) the equivalent plastic strain, (b) Von-Mises stress, and (c) σ_{zz} for the SEMVEs with varying aspect ratios.

Table 5 Scaled mean, standard deviation, and extreme value of the aggregated equivalent plastic strain, Von-Mises stress, and σ_{zz} for SEMVEs with varying ellipsoidal void orientations: (i) Euler angles in case 4 (horizontal), (ii) Euler angles in case 5 (45 °), and (iii) Euler angles in case 6 (vertical).

	Orientation for case 4	Orientation for case 5	Orientation for case 6
$\bar{\mu}^{EPS}$	0.97802	0.99075	1.0049
$\bar{\sigma}^{EPS}$	10.8326	7.1038	2.4837
$\bar{F}(0.99)^{EPS}$	2.4558	1.8711	1.2996
$\bar{\mu}^{VM}$	0.9955	0.99822	0.99926
$\bar{\sigma}^{VM}$	1.2186	1.099	1.0113
$\bar{F}(0.99)^{VM}$	1.0179	1.0076	0.99822
$\bar{\mu}^{LC}$	0.95141	0.97291	0.99725
$\bar{\sigma}^{LC}$	3.0904	2.4593	1.3249
$\bar{F}(0.99)^{LC}$	1.2016	1.1443	1.0333

effect on the PDFs than elongated voids which dominate the LOF voids. This aligns well with experimental measurements in [29].

The results of this analysis demonstrate that spherical voids have a significantly lower effect on the PDFs of state variables than voids that are elongated on a per-volume fraction basis. From the physics of the melting process, orientation of voids due to either lack of fusion or keyholing can cause significant anisotropy in material response if there is a strong bias of elongated voids in one direction. However even without anisotropy in the pore orientation, the overall effect of elongated voids is greater on the PDFs of state variables than more spherical voids, even for the same volume fraction.

7. Conclusion

This paper builds a comprehensive image-based statistically equivalent microstructural volume element (SEMVE) and associated crystal plasticity constitutive relations for efficient micromechanical simulation of AM-processed Ti-6Al-4V alloys characterized by Widmanstätten morphology containing 12 HCP α lath variants. A major step towards gaining significant efficiency is the creation of an effective crystal plasticity framework for parent β grains with a parametric representation of α lath size, shape, orientation, and crystallography statistics. The development identifies the crystallographic relationship of α laths with respect to their parent β grains, and deploys a method to incorporate

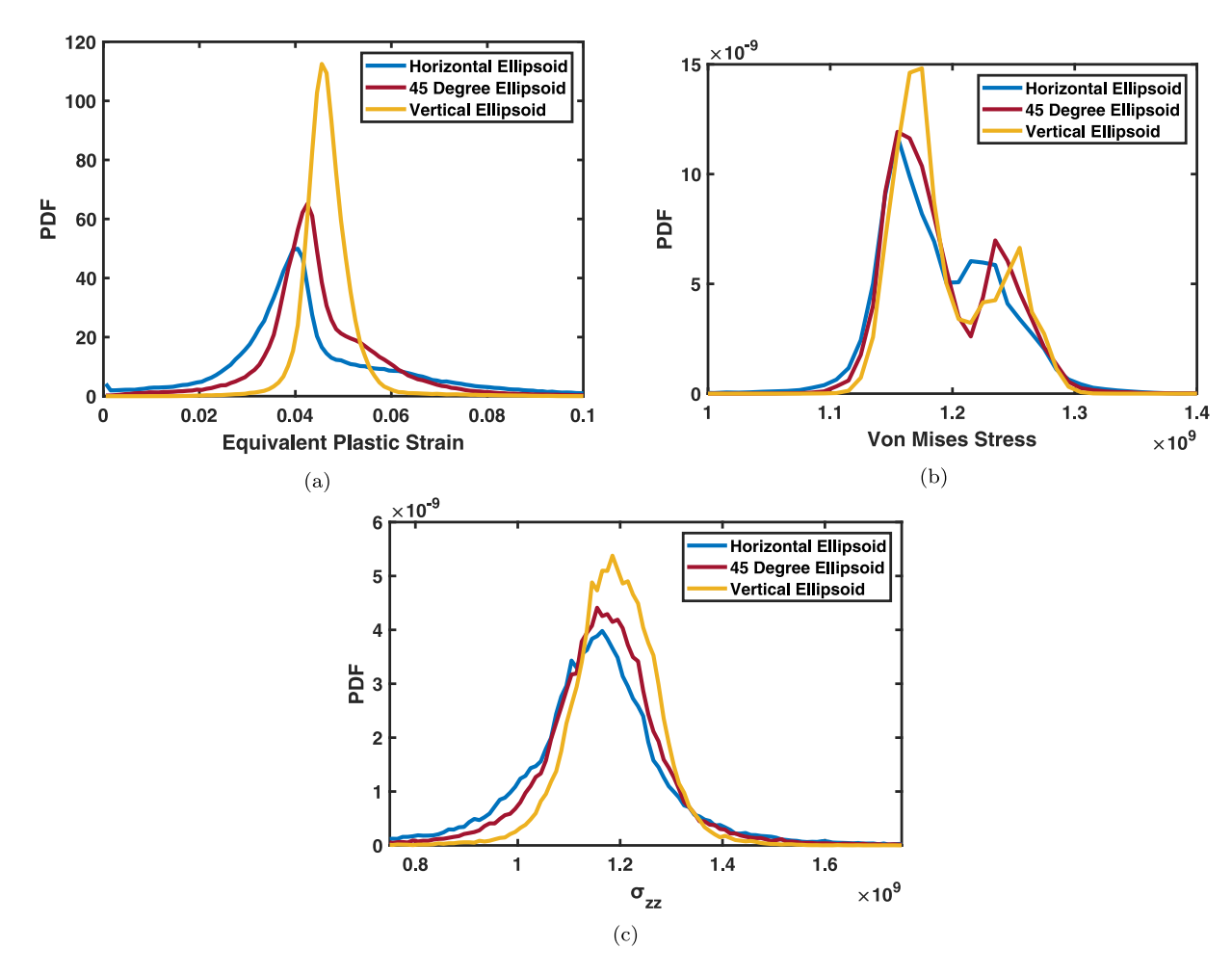


Fig. 15. The aggregated PDFs (over 5 instantiations) of (a) the equivalent plastic strain, (b) Von-Mises stress, and (c) σ_{zz} for the cases 4 (horizontal), 5 (45°), and 6 (vertical) with ellipsoidal voids and varying orientations.

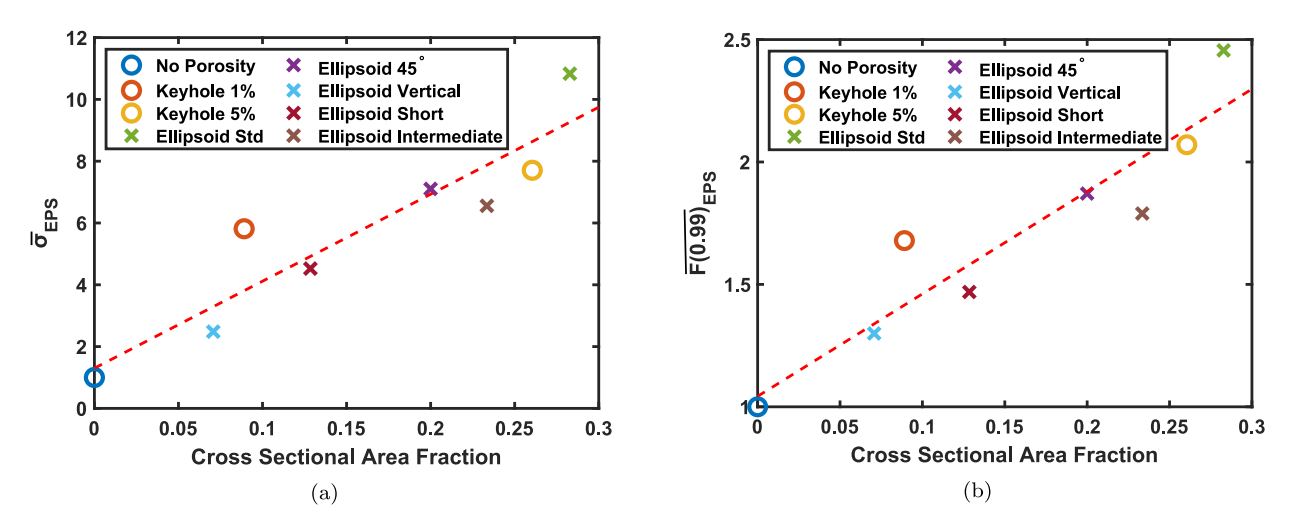


Fig. 16. Plot of (a) $\bar{\sigma}^{EPS}$ and (b) $\bar{F}(0.99)^{EPS}$ as a function of the cross-sectional area of the void in the SEMVE ($R^2 = 0.8504$) for each morphological case in Table 2, showing a smaller effect of spherical voids than elongated voids.

a parametric representation of α lath statistics in β grains. It is expected that this implicit representation will significantly enhance its efficiency over other models that represent each α lath explicitly in the microstructure.

3D ellipsoidal shapes are assumed for the α laths. The statistical representation process generates a set of most probable ellipsoids through the use of stereology principles on the observed EBSD images and constructs statistical functions that characterize the distribution of

Table A.6
Slip system dependent parameters in Section 4.

Parameter	Basal	Prismatic	< a > Pyramidal	< c + a > Pyramidal I & II
θ_{ref}	300 °K	300 °K	300 °K	300 °K
$\hat{\theta}_{ref}$	400 °K	200 °K	200 °K	160 °K
h_0	150 MPa	150 MPa	150 MPa	150 MPa
\widetilde{g}	470 MPa	570 MPa	570 MPa	1550 MPa
\bar{g}	241 MPa	236 MPa	360 MPa	466 MPa
c_1	0.08	0.062	0.07	0.05
c_2	1	1	1	1

Table A.7 Additional material constants in the crystal plasticity model of Section 4.

Parameter	Value	
K	.162 $\frac{MPa}{m^{0.5}}$	
G	48 GPa	
Q	2.5^{-19} J	
c	500 MPa	
d	100	

the resulting 3D ellipsoids. A grain reconstruction algorithm is subsequently executed, allowing for the identification of the crystallographic orientation of parent β grains. The morphology of β grains is quantified and an algorithm is developed with the DREAM.3D software to generate statistically equivalent instantiations of the β grain microstructure.

The crystal plasticity model also accounts for porosity evolution in the microstructure. The model is calibrated and validated with results from tests performed on AM-processed Ti-6Al-4V KH1 and stock samples. A contribution of this paper is the development of the self-consistent boundary condition that are implemented through embedding the SEMVE in a homogenized exterior domain in a concurrent model. This boundary condition is necessary to overcome the limitations of periodicity boundary conditions in modeling larger specimens. The exterior domain in the concurrent model is modeled by an isotropic rate-dependent plasticity model (IRDPM) that is calibrated from the microstructural CPFE model. Experimental boundary conditions are applied on the exterior boundary of the concurrent model, thereby facilitating the simulation of experimental specimens.

Parametric studies are finally conducted with this model to examine the effect of the larger void size, shape, and orientation on the mechanical response of the SEMVEs. The studies conclude that a simple volume fraction-based approach to characterizing the effect of void defects on the spatial distribution of state variables is insufficient. Aspect ratios and orientation are equally important for determining the overall effect on the material response. In summary, this paper has developed a robust and unique platform that can be effectively used to model additively manufactured metallic materials with complex microstructures undergoing a variety of loading conditions.

CRediT authorship contribution statement

M. Pinz: Investigation, Methodology, Software, Formal analysis, Visualization, Writing – original draft. S. Storck: Investigation, Methodology, Formal analysis, Writing – review & editing. T. Montalbano: Investigation, Methodology. B. Croom: Investigation, Methodology.
N. Salahudin: Methodology, Formal analysis. M. Trexler: Methodology, Resources, Supervision. S. Ghosh: Conceptualization, Investigation, Methodology, Supervision, Writing – review & editing, Project administration, Funding acquisition.

Declaration of competing interest

The authors declare that they have no known competing financial interests or personal relationships that could have appeared to influence the work reported in this paper.

Data availability

Data will be made available on request.

Acknowledgments

This work has been supported through a grant from the National Science Foundation, Mechanics of Materials and Structures (MOMS) Program (grant no. CMMI-1825115 Program Manager: Dr. Siddiq Qidwai) and a grant from the NASA Transformational Tools and Technologies (TTT) Program (award no. 80NSSC21M0097). The authors thank Dr. Ed Glaessgen of NASA LaRC for program support and insights. This work was carried out at the Advanced Research Computing at Hopkins (ARCH) core facility (rockfish.jhu.edu), which is supported by the AFOSR DURIP grant FA9550-21-1-0303. Additional computational support was provided by the Extreme Science and Engineering Discovery Environment (XSEDE) bridges-2 cluster at the Pittsburgh Supercomputing Center (PSC) is also gratefully acknowledged.

Appendix A. Calibrated crystal plasticity parameters

The interaction matrices between slip systems are given by the following parameters: $\tilde{q}^{\alpha\beta}=1$, $\chi_{AF}^{\alpha\beta}=1$, and $\chi_{AP}^{\alpha\beta}=1$ for all slip system pairs (see Table A.6 and Table A.7).

Appendix B. Rate-dependent isotropic plasticity model (RDIPM) parameters

The table for the rate-dependent isotropic plasticity model (RDIPM) parameters for the exterior domain is given in Table B.8.

Appendix C. Method for perturbing statistics of size, aspect ratio and orientation

The beta distributions with parameters $(a_{AB},b_{AB},a_{AC},b_{AC})$ for the B/A and C/A aspect ratios are randomly sampled a large number of times (1000 for this example) with values in the interval [0,1]. These are then inverted so they then represent A/C, and A/B ratios. Two random numbers u and v are generated from a uniform pseudo-random number generator between 0 and 1. Each element x within the sampled A/C list is modified as $x^* = (x-1)(1-2pfloor(u,0.5)+p)$ where p is a perturbation factor (set to 0.1). Subsequently, the modified x^* sample aspect ratios are inverted back to C/A so that they are again between 0 and 1. A beta distribution is fit to the modified $1/x^*$ samples, and the new parameters are included in the trial parameters $S_{1D}^{(p)}$.

Table B.8
RDIPM parameters in Section 5

RDIPM parameters in Section 5.	
Parameter	Value
$ar{Y_0}$	1.68 GPa
$egin{array}{c} ar{Y}_0 \ ar{eta} \end{array}$	3 10-3
$ar{H}$	1.75 GPa
$\hat{\alpha}$	400 MPa
ψ	1
a	2
m	0.0105

References

- W. Chen, Z. Li, Additive manufacturing of titanium aluminides, in: F. Froes, B. Boyer (Eds.), Additive Manufacturing for the Aerospace Industry, Elsevier, 2019, pp. 235–263.
- [2] M. Seifi, M. Gorelik, J. Waller, N. Hrabe, N. Shamsaei, S. Daniewicz, J.J. Lewandowski, Progress towards metal additive manufacturing standardization to support qualification and certification, JOM 69 (3) (2017) 439–455.
- [3] B. Boyce, B. Salzbrenner, J. Rodelas, A. Roach, L. Swiler, J. Madison, B. Jared, Y.-L. Shen, Extreme value statistics reveal rare failure-critical defects in additive manufacturing, Adv. Eng. Mater. 19 (8) (2017) 1700102.
- [4] B. Salzbrenner, J. Rodelas, Y.-L. Shen, J. Madison, B. Jared, L. Swiler, B. Boyce, High-throughput stochastic tensile performance of additively manufactured stainless steel, J. Mater. Proc. Tech. 241 (2017) 1–12.
- [5] M. Kasemer, M.P. Echlin, J.C. Stinville, T.M. Pollock, P. Dawson, On slip initiation in equiaxed α/β Ti-6Al-4V, Acta Mater. 136 (2017) 288–302.
- [6] J. Mayeur, D. McDowell, A three-dimensional crystal plasticity model for duplex Ti-6Al-4V, Int. J. Plast. 23 (9) (2007) 1457–1485.
- [7] J.R. Mayeur, D.L. McDowell, R.W. Neu, Crystal plasticity simulations of fretting of Ti-6Al-4V in partial slip regime considering effects of texture, Comput. Mater. Sci. 41 (3) (2008) 356–365.
- [8] K. Chatterjee, M.P. Echlin, M. Kasemer, P.G. Callahan, T.M. Pollock, P. Dawson, Prediction of tensile stiffness and strength of Ti-6Al-4V using instantiated volume elements and crystal plasticity, Acta Mater. 157 (2018) 21–32.
- [9] D. Hu, J. Pan, J. Mao, X. Guo, H. Ji, R. Wang, An anisotropic mesoscale model of fatigue failure in a titanium alloy containing duplex microstructure and hard α inclusions, Mater. Des. 193 (2020) 108844.
- [10] J. Thomas, M.A. Groeber, S. Ghosh, Image-based crystal plasticity FE analysis for microstructure dependent properties of Ti-6Al-4V alloys, Mater. Sci. Engin. A 553 (2012) 164–175.
- [11] M. Seifi, A. Salem, J. Beuth, O. Harrysson, J.J. Lewandowski, Overview of materials qualification needs for metal additive manufacturing, JOM 68 (3) (2016) 747–764.
- [12] R. Cunningham, A. Nicolas, J. Madsen, E. Fodran, E. Anagnostou, M. Sangid, A. Rollett, Analyzing the effects of powder and post-processing on porosity and properties of electron beam melted Ti-6Al-4V, Mater. Res. Lett. 5 (2017) 516–525.
- [13] K. Kapoor, Y.S.J. Yoo, T.A. Book, J.P. Kacher, M.D. Sangid, Incorporating grain-level residual stresses and validating a crystal plasticity model of a two-phase Ti-6Al-4 V alloy produced via additive manufacturing, J. Mech. Phys. Sol. 121 (2018) 447–462.
- [14] P. Liu, Z. Wang, Y. Xiao, R. Lebensohn, Y. Liu, M. Horstemeyer, X. Cui, L. Chen, Integration of phase-field model and crystal plasticity for the prediction of process-structure- property relation of additively manufactured metallic materials, Int. J. Plast. 128 (2020) 102670.
- [15] K. Somlo, K. Poulios, C. Funch, C. Niordson, Anisotropic tensile behaviour of additively manufactured Ti-6Al-4V simulated with crystal plasticity, Mech. Mater. 162 (2021) 104034.
- [16] F. Azhari, C. Wallbrink, Z. Sterjovski, B. Crawford, A. Menzel, D. Agius, C. Wang, G. Schaffer, Predicting the complete tensile properties of additively manufactured Ti-6Al-4V by integrating three-dimensional microstructure statistics with a crystal plasticity model. Int. J. Plast. 148 (2022) 103127.
- [17] R. Shi, Y. Wang, Variant selection during α precipitation in Ti–6Al–4V under the influence of local stress: A simulation study, Acta Mater. 61 (16) (2013) 6006–6024.
- [18] R. Shi, N. Zhou, S. Niezgoda, Y. Wang, Microstructure and transformation texture evolution during α precipitation in polycrystalline α/β titanium alloys–A simulation study, Acta Mater. 94 (2015) 224–243.
- [19] J. Zhang, X. Li, D. Xu, C. Teng, H. Wang, L. Yang, H. Ju, H. Xu, Z. Meng, Y. Ma, et al., Phase field simulation of the stress-induced α microstructure in Ti–6Al–4 V alloy and its CPFEM properties evaluation, J. Mater. Sci. Tech. 90 (2021) 168–182.
- [20] B. Radhakrishnan, S. Gorti, S.S. Babu, Phase field simulations of autocatalytic formation of alpha lamellar colonies in Ti-6Al-4V, Metal. Mater. Trans. A 47 (12) (2016) 6577–6592.
- [21] M. Pinz, J. Benzing, A. Pilchak, S. Ghosh, A microstructure-based porous crystal plasticity FE model for additively manufactured Ti-6Al-4V alloys, Int. J. Plast. 153 (2022) 103254.
- [22] M.M. Francois, A. Sun, W.E. King, N.J. Henson, D. Tourret, C.A. Bronkhorst, N.N. Carlson, C.K. Newman, T.S. Haut, J. Bakosi, J.W. Gibbs, V. Livescu, S.A. Vander Wiel, A.J. Clarke, M.W. Schraad, T. Blacker, H. Lim, T. Rodgers, S. Owen, F. Abdeljawad, J. Madison, A.T. Anderson, J.L. Fattebert, R.M. Ferencz, N.E. Hodge, S.A. Khairallah, O. Walton, Modeling of additive manufacturing processes for metals: Challenges and opportunities, Curr. Opin. Solid State Mater. Sci. 21 (4) (2017) 198–206.
- [23] L.-X. Lu, N. Sridhar, Y.-W. Zhang, Phase field simulation of powder bed-based additive manufacturing. Acta Mater. 144 (2018) 801–809.
- [24] N. Shamsaei, A. Yadollahi, L. Bian, S.M. Thompson, An overview of direct laser deposition for additive manufacturing; Part II: Mechanical behavior, process parameter optimization and control, Add. Manufac. 8 (2015) 12–35.

- [25] Q. Yang, S. Ghosh, A crystal plasticity model for porous HCP single crystal titanium alloys under multiaxial loading conditions, Int. J. Sol. Struct. 61 (16) (2021) 6006–6024.
- [26] M. Pinz, G. Weber, J.C. Stinville, T. Pollock, S. Ghosh, Data-driven Bayesian model-based prediction of fatigue crack nucleation in Ni-based superalloys, NPJ Comput. Mater. 8 (1) (2022) 1–15.
- [27] G. Weber, M. Pinz, S. Ghosh, Machine learning-enabled self-consistent parametrically-upscaled crystal plasticity model for Ni-based superalloys, Comput. Methods Appl. Mech. Engrg. (2022) 115384.
- [28] W. Burgers, On the process of transition of the cubic-body-centered modification into the hexagonal-close-packed modification of zirconium, Physica 1 (7–12) (1934) 561–586.
- [29] T. Montalbano, B.N. Briggs, J.L. Waterman, S. Nimer, C. Peitsch, J. Sopcisak, D. Trigg, S. Storck, Uncovering the coupled impact of defect morphology and microstructure on the tensile behavior of Ti-6Al-4V fabricated via laser powder bed fusion, J. Mater. Proc. Tech. 294 (2021) 117113.
- [30] C. Cepeda-Jiménez, F. Potenza, E. Magalini, V. Luchin, A. Molinari, M. Pérez-Prado, Effect of energy density on the microstructure and texture evolution of Ti-6Al-4V manufactured by laser powder bed fusion, Mater. Character. 163 (2020) 110238.
- [31] R. Zhao, C. Chen, C. Wang, T. Cao, S. Shuai, S. Xu, T. Hu, H. Liao, J. Wang, Z. Ren, On the role of volumetric energy density in the microstructure and mechanical properties of laser powder bed fusion Ti-6Al-4V alloy, Additive Manuf. 51 (2022) 102605.
- [32] M.A. Groeber, M.A. Jackson, DREAM. 3D: A digital representation environment for the analysis of microstructure in 3D, Int. Mater. Manuf. Innov. 3 (1) (2014) 56–72.
- [33] VGSTUDIO MAX Suite, Volume Graphics Inc., 2021.
- [34] M. Pinz, G. Weber, W. Lenthe, M. Uchic, T. Pollock, S. Ghosh, Microstructure and property based statistically equivalent RVEs for intragranular γ- γ'microstructures of Ni-based superalloys, Acta Mater. 157 (2018) 245–258.
- [35] A. Bagri, G. Weber, J.-C. Stinville, W. Lenthe, T. Pollock, C. Woodward, S. Ghosh, Microstructure and property-based statistically equivalent representative volume elements for polycrystalline Ni-based superalloys containing annealing twins, Metal. Mater. Trans. A 49 (11) (2018) 5727–5744.
- [36] S. Ghosh, D.V. Kubair, Exterior statistics based boundary conditions for representative volume elements of elastic composites, J. Mech. Phys. Solids 95 (2016) 1–24.
- [37] B. Song, S. Dong, B. Zhang, H. Liao, C. Coddet, Effects of processing parameters on microstructure and mechanical property of selective laser melted Ti-6Al-4V, Mater. Des. 35 (2012) 120–125.
- [38] C. Cayron, GenOVa: A computer program to generate orientational variants, J. App. Cryst. 40 (6) (2007) 1179–1182.
- [39] A. Zaitzeff, A. Pilchak, T. Berman, J. Allison, S. Esedoglu, A robust algorithm to calculate parent β grain shapes and orientations from α phase electron backscatter diffraction data in α/β-titanium alloys, Scr. Mater. 191 (2021) 191–195.
- [40] G. Lütjering, J.C. Williams, Titanium, Springer Science & Business Media, 2007.
- [41] X. Tu, A. Shahba, J. Shen, S. Ghosh, Microstructure and property based statistically equivalent RVEs for polycrystalline-polyphase aluminum alloys, Inter. Jour. Plast. 115 (2019) 268–292.
- [42] M.A. Groeber, S. Ghosh, M.D. Uchic, D. Dimiduk, A framework for automated analysis and representation of 3D polycrystalline microstructures, Part 1: Statistical characterization, Acta Mater. 56 (6) (2008) 1257–1273.
- [43] M.A. Groeber, S. Ghosh, M.D. Uchic, D. Dimiduk, A framework for automated analysis and representation of 3D polycrystalline microstructures, Part 2: Synthetic structure generation, Acta Mater. 56 (6) (2008) 1274–1287.
- [44] A.W. Bowman, A. Azzalini, Applied Smoothing Techniques for Data Analysis: The Kernel Approach with S-Plus Illustrations, Vol. 18, OUP Oxford, 1997.
- [45] R. Hielscher, MTEX http://mtex-toolbox.github.io/. 2021.
- [46] D. Deka, D.S. Joseph, S. Ghosh, M.J. Mills, Crystal plasticity modeling of deformation and creep in polycrystalline Ti-6242, Metal. Mater. Trans. A 37 (5) (2006) 1371–1388.
- [47] S. Kotha, D. Ozturk, S. Ghosh, Parametrically homogenized constitutive models (PHCMs) from micromechanical crystal plasticity FE simulations, Part I: Sensitivity analysis and parameter identification for titanium alloys, Int. J. Plast. 120 (2019) 296–319.
- [48] D. Ozturk, A. Shahba, S. Ghosh, Crystal plasticity FE study of the effect of thermo-mechanical loading on fatigue crack nucleation in titanium alloys, Fat. Fract. Eng. Mater. Struct. 39 (6) (2016) 752-769.
- [49] G. Venkataramani, K. Kirane, S. Ghosh, Microstructural parameters affecting creep induced load shedding in Ti-6242 by a size dependent crystal plasticity FE model, Int. J. Plast. 24 (3) (2008) 428–454.
- [50] M. Ashby, The deformation of plastically non-homogeneous materials, Phil. Mag.: J. Theor. Exper. Appl. Phys. 21 (170) (1970) 399–424.
- [51] Simulation Modeling Suite, Simmetrix Inc., 2015.
- [52] M.E. Gurtin, E. Fried, L. Anand, The Mechanics and Thermodynamics of Continua, Cambridge University Press, 2010.
- [53] E. Voce, A practical strain hardening function, Metallurgia 51 (1955) 219-226.